Polycrystalline exchange-biased bilayers: Magnetically effective versus structural antiferromagnetic grain volume distribution

Maximilian Merkel,* Meike Reginka, Rico Huhnstock, and Arno Ehresmann†
Institute of Physics and Center for Interdisciplinary Nanostructure Science and Technology (CINSaT), University of Kassel, Heinrich-Plett-Strasse 40, 34132 Kassel, Germany

(Received 8 April 2022; revised 9 June 2022; accepted 24 June 2022; published 7 July 2022)

The magnetic characteristics of polycrystalline exchange-biased antiferromagnet/ferromagnet bilayers are determined by a complex interplay of parameters, describing structural and magnetic properties of the material system, including, in particular, the grain volume distribution of the antiferromagnet. An ideal characterization of such systems would be a nondestructive determination of the relevant parameters for each individual grain. This is in most cases not feasible, since typical characterization methods average over larger areas. Here, we show that it is, however, possible to determine averaged microscopic parameters from averaged macroscopic magnetic quantities measured by vectorial Kerr magnetometry in comparison to an elaborate model. In particular, we estimate the magnetically effective antiferromagnetic grain size distribution, being essential for the interface exchange coupling to the ferromagnetic layer. We found that the distribution of magnetically active grain sizes differs from the structural one, indicating that the antiferromagnetic order, relevant for the exchange bias, extends only over a part of the grains' structural volumes.

DOI: 10.1103/PhysRevB.106.014403

I. INTRODUCTION

An antiferromagnet (AFM) and a ferromagnet (FM) sharing an interface in a thin bilayer system commonly results in a horizontal shift of the ferromagnetic hysteresis loop accompanied by an additional modification of its coercivity as compared with loops of a pure FM [1–3]. With the effect arising from exchange interaction across the common interface, the phenomenon has been named exchange bias (EB) and is a key effect for the development of data storage and magnetic sensor technology [4–7]. Furthermore, domain engineering of polycrystalline EB thin films [8–13] has proven to be an important ingredient of lab-on-a-chip devices [14] enabling the actuation of magnetic particles in liquid media [15–17].

The exchange bias shift H_{EB} is caused by an interaction of the FM magnetic moments with uncompensated interface moments of the AFM layer. It is interpreted as a consequence of a macroscopic unidirectional magnetic anisotropy (UDA), resulting from an aligned pinning of the FM spins to the AFM ones [1,18]. The modification of the coercivity H_{C} is attributed to rotatable AFM moments resulting in a dynamic rotatable magnetic anisotropy (RMA) [18,19]. In polycrystalline systems, these anisotropies are—apart from the AFM/FM interface [20,21] and the AFM crystal structure [22,23]—mainly determined by the grain volume distribution (GVD) of the AFM [3,24–26]. A general description of the EB in polycrystalline systems has solidified over the last decades [3,8,25,27,28], connecting the AFM GVD with the macroscopically observable features by subdividing the AFM ensemble into classes of grains differently responding to rotating FM magnetic moments during their reversal. The grains exhibit a varying thermal stability with respect to the reorientation of their uncompensated magnetic interface moment upon the FM layer's remagnetization. For given temperature and duration of observation, AFM grains can be classified to contribute to the macroscopic UDA or RMA [3,25,28]. In addition to the grain-specific magnetic anisotropy and exchange coupling constant, the interaction of an AFM grain with the FM magnetic moments is determined by the ratio of the interface area, mediating the coupling, and the magnetically effective AFM grain volume [8,27]. For columnar AFM grains and assuming that the magnetic anisotropy extends over their complete structural volumes, this relates to the grain-specific aspect ratio of cylindrical AFM grains, scaling directly with the AFM layer thickness for thin layers [3,29].

One—to the knowledge of the authors—hitherto unanswered question is whether the structural GVD is identical to the distribution of the magnetically active AFM grain volumes. Therefore a quantitative link between the magnetic characteristics of polycrystalline AFM/FM bilayers and their microstructure is crucial, even if the connection between thickness-dependent relations of H_{EB} and H_{C} and the AFM layer's granular characteristic, or the nature of the EB as an interface effect itself, can be reasoned [3,29–33].

We present systematic thickness-dependent investigations of H_{EB} and H_{C} in the case of columnar grain growth, which we could validate by grain size analysis by means of atomic force microscopy. A quantitative connection between the averaged macroscopic magnetic characteristics and averaged microscopic material parameters is established by comparing thickness-dependent measurements with model calculations utilizing an extended time-dependent Stoner-Wohlfarth (SW) approach [26,28]. In conjunction, analytic expressions for the thickness-dependent relations were derived in the context

*max.merkel@physik.uni-kassel.de
†ehresmann@physik.uni-kassel.de

of a generalized description of polycrystalline EB systems [3,25,28], which further solely depend on measurement conditions and parameters characterizing the averaged microscopic properties of the system.

II. EXPERIMENT

Prototypical AFM/FM-bilayer systems of the type $Si(100)/Cu^{5nm}/Ir_{17}Mn_{83}^{t_{AFM}}/Co_{70}Fe_{30}^{t_{FM}}/Si^{20nm}$ were fabricated on naturally oxidized Si by rf-sputter deposition at room temperature of alloy targets with the same compositions. Different nominal thicknesses t_{AFM} between 2.5 and 50 nm with fixed $t_{FM} = 10$ nm and different t_{FM} between 5 and 30 nm at fixed $t_{AFM} = 5$ and 30 nm were prepared. Deposition rates were $\eta_{Cu} = (6.7 \pm 0.2)$ nm/min, $\eta_{IrMn} = (5.5 \pm 0.8)$ nm/min, $\eta_{CoFe} = (3.40 \pm 0.13)$ nm/min, and $\eta_{Si} = (3.84 \pm 0.96)$ nm/min for all layers, determined as described in Ref. [26]. Furthermore, an unbiased FM sample with $t_{FM} = 10$ nm was fabricated as a reference by omitting the AFM layer ($t_{AFM} = 0$ nm). The base pressure was $< 10^{-6}$ mbar, the working pressure was $\approx 10^{-2}$ mbar, and during deposition an in-plane magnetic field set to 28 kA/m was applied. While the 20-nm Si capping layer serves as oxidation protection and further enhances the contrast in the magneto-optical measurements [28], the 5-nm Cu buffer layer induces the desired (111) texture in the IrMn layer [22,26].

For the determination of the distribution $\tilde{\varrho}(r_{AFM})$ of AFM surface grain radii r_{AFM} at thicknesses t_{AFM} between 5 and 100 nm, the FM and capping layer have been omitted. Similarly, for samples with $t_{FM} = 10$ nm as well as $t_{AFM} = 5$ and 30 nm, the capping layer has been omitted to determine the FM grain surface radius distribution $\tilde{\varrho}(r_{FM})$. For tuning the average aspect ratio of AFM grains, the layer stack has been fabricated with different AFM deposition rates from 0.9 to 6.8 nm/min for samples with t_{AFM} between 2.5 and 50 nm at fixed $t_{FM} = 10$ nm.

The distributions of grain radii were determined by atomic force microscopy in contact mode measuring several spots on the samples' surface with a nominal resolution of 0.49 nm/pixel. Utilizing the watershed algorithm provided by the evaluation software GWYDDION (v.2.51) [34], the surface topography was analyzed applying the same evaluation procedure as described in Ref. [26].

The samples were magnetically characterized by vectorial magneto-optical Kerr magnetometry as described in Ref. [28]. Magnetization reversal curves were obtained for angles between $\varphi = 0°$ and 360° with an increment of 1°, where φ is the angle between the magnetic field applied during layer growth and the field applied during the measurements. φ has been corrected by considering $H_C^{exp}(\varphi)$ to be largest at $\varphi = 0°$ and 180° with an accuracy of 1° in accordance to Refs. [26,28,35]. The magnetization curves shared a sweep rate of $\nu \approx 7.27$ kA/ms and a resolution of $\Delta H \approx 0.53$ kA/m resulting in a measurement time of $t_{Hys} \approx 44$ s. The EB shift H_{EB}^{exp} and the coercive field H_C^{exp} are derived from the zero crossings H_{asc} and H_{desc} of the ascending and descending branch of the recorded angle-specific hysteresis loops, respectively, via $H_{EB}^{exp} = (H_{asc} + H_{desc})/2$ and $H_C^{exp} = (H_{asc} - H_{desc})/2$ starting out from positive saturation [26].

III. POLYCRYSTALLINE MODEL

A. General description

The physical interpretation of the experimental results will be performed within the model for polycrystalline EB systems [3,8,18,25–28,36]. The phenomenon is condensed down to the interaction between a uniform FM layer and a granular AFM [3]. An individual AFM grain i with a magnetically effective volume $V_{AFM,i}$, not necessarily identical to the actual physical volume, and an anisotropy constant $K_{AFM,i}$ interacting with the FM at the shared interface $A_{AFM,i}$ via exchange interaction described by the microscopic exchange energy area density $J_{EB,i}$ possesses an energy barrier [8,27]

$$\Delta E_{AFM,i} = K_{AFM,i} V_{AFM,i} - J_{EB,i} A_{AFM,i} \left(1 - \frac{J_{EB,i} A_{AFM,i}}{4 K_{AFM,i} V_{AFM,i}}\right) \quad (1)$$

between two energy minima corresponding to the parallel (global minimum) and antiparallel (local minimum) alignment of the grain-averaged uncompensated AFM interface magnetic moment $\vec{m}_{AFM,i}$ with respect to $\vec{M}_{FM}$ representing the FM magnetization. Equation (1) is in first order given by $\Delta E_{AFM,i} \approx K_{AFM,i} V_{AFM,i}$ [3,8,27]. This allows for a connection of the AFM GVD $\varrho(V_{AFM})$ with the distribution of relaxation times $\tau_{AFM,i} = \tau_0 \exp\{\Delta E_{AFM,i}/k_B T\}$ with $\nu_0 = 1/\tau_0$ as the characteristic frequency for spin reversal of the AFM grains, T representing the observation temperature, and k_B as Boltzmann's constant [3,28].

For given measurement and storage temperatures and times, AFM grains can be classified with respect to their thermal stability, i.e., their individual energy barriers $\Delta E_{AFM,i}$ and consequently relaxation times $\tau_{AFM,i}$, directly related to the individual grain volumes $V_{AFM,i}$ for constant $K_{AFM,i}$ [Fig. 1(a)] [3,26–28]. A constant $K_{AFM,i} = K_{AFM}\ \forall i$ is an assumption possibly not valid for very small grain sizes [37]. Thermally unstable grains of classes I and II either exhibit superparamagnetic behavior (class I) or have relaxation times of the order of the observation time (class II), which is in typical experiments equivalent to the hysteresis duration t_{Hys} [19,25,28]. Grains of class II are called rotatable, describing a realignment of the grain-averaged uncompensated AFM interface magnetic moment during the FM's remagnetization and consequently having an effect on the coercivity H_C [19,36]. Grains of classes III and IV are thermally stable with relaxation times larger than t_{Hys} on the timescale of observation. Class III grains are the origin of the macroscopically observable EB shift H_{EB} because they have been aligned by an initialization procedure (e.g., postannealing) [1,3,26], via applying an adequately strong external magnetic field during deposition [25,26] or during an ion bombardment [8,38–40], by thermally assisted scanning probe lithography [13], or via laser-based annealing [11,12,41]. The orientation of the uncompensated AFM moments of class IV grains cannot be set by one of the named treatments, and their pinning directions are assumed to be randomly distributed [3,28]. Grains of classes II and III are assumed to be superposable with respect to their uncompensated interface moments, macroscopically resulting in a RMA mediating H_C [19,25,28] and a UDA mediating H_{EB} [3,28], respectively.

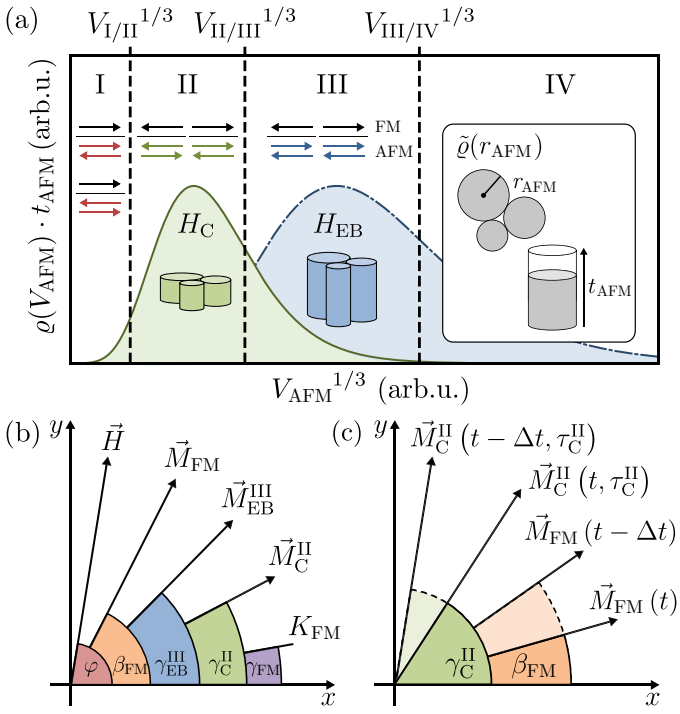

FIG. 1. (a) Distributions $\varrho(V_{AFM})$ of AFM grain volumes V_{AFM} schematically depicted for a thin (green, solid line) and a thick AFM layer (blue, dash-dotted line) assuming a constant distribution of AFM grain radii for different t_{AFM}, i.e., homogeneous columnar grain growth. The distributions are divided into four classes of different thermal stability by boundaries $V_{I/II}$, $V_{II/III}$, and $V_{III/IV}$ connected to material parameters and conditions during observation and post-treatment. Colored antiparallel arrows (⇆ and ⇄) schematically depict uncompensated AFM grain-averaged magnetic moments of the respective grain class interacting with the reversing FM magnetization represented by black arrows (← and →). Inset: Schematic top view of columnar grains with different sizes connected to the distribution $\tilde{\varrho}(r_{AFM})$ of AFM grain radii r_{AFM} and the scaling of individual grain volumes for fixed r_{AFM} with t_{AFM}. (b) Vectors in the applied extended SW approach and corresponding angles with respect to an arbitrary reference frame. $\vec{H}$ is the external magnetic field with its azimuthal angle φ, $\vec{M}_{FM}$ is the FM magnetization with the angle β_{FM}, K_{FM} is the energy density of the ferromagnetic uniaxial magnetic anisotropy (FUMA) with its easy direction defined by γ_{FM}, $\vec{M}_C^{II}$ and $\vec{M}_{EB}^{III}$ are the superposed uncompensated magnetic moments related to AFM grains of classes II and III with γ_C^{II} and γ_{EB}^{III} as the corresponding azimuthal angles connected to the RMA and the UDA, respectively. (c) Illustration of the RMA during a magnetization reversal of the FM at time steps t and $t-\Delta t$ visualizing the continuous relaxation of $\vec{M}_C^{II}$ into a state parallel to $\vec{M}_{FM}$. (b) and (c) are adapted from Ref. [36].

B. Grain size distribution and class boundaries

The grain size distribution of sputtered polycrystalline thin films is typically found to be lognormal [Fig. 1(a)] [3,24,42–44]. For a polycrystalline AFM layer of thickness t_{AFM} we assume cylindrical, homogeneously grown grains [26] with radius r_{AFM} and volume V_{AFM} [Fig. 1(a)]. The AFM GVD can be calculated from the lognormally distributed grain radii $\tilde{\varrho}(r_{AFM},\mu,\sigma)$ via a change in variables giving

$$\varrho(V_{AFM},t_{AFM},\mu,\sigma)=\tilde{\varrho}(r_{AFM}(V_{AFM}),\mu,\sigma)\partial_{V_{AFM}}r_{AFM}(V_{AFM})$$
$$=\frac{\tilde{\varrho}(\sqrt{V_{AFM}/\pi t_{AFM}},\mu,\sigma)}{2\sqrt{\pi V_{AFM}t_{AFM}}} \quad (2)$$

with $r_{AFM}(V_{AFM})=\sqrt{V_{AFM}/\pi t_{AFM}}$ [3,26,37,45]. μ and σ represent the parameters characterizing the lognormal distribution with respect to r_{AFM}. The expectation value $\langle r_{AFM}\rangle$ of the grain radius as well as the standard deviation SD are given by $\langle r_{AFM}\rangle=\exp\{\mu+\sigma^2/2\}$ and $\mathrm{SD}=\langle r_{AFM}\rangle\sqrt{\exp\{\sigma^2\}-1}$ [24]. With Eq. (2) and as shown in Fig. 1(a), $\varrho(V_{AFM},t_{AFM},\mu,\sigma)$ can be modified with respect to the grain class boundaries by varying t_{AFM} for a fixed distribution $\tilde{\varrho}(r_{AFM},\mu,\sigma)$.

The boundaries between the grain classes are functions of temperature and time [3] and can be estimated via [37]

$$V_{AFM}(T,\tau)=\frac{k_BT}{K_{AFM}(T)}\ln\left\{\frac{\tau}{\tau_0}\right\}. \quad (3)$$

For hysteresis curve measurements, the boundary $V_{II/III}$ between classes II and III [Fig. 1(a)] is determined by the measurement temperature $T=T_{RT}$ (where T_{RT} is room temperature) and the hysteresis duration $\tau=t_{Hys}$. $V_{III/IV}$ is determined by $T=T_{ini}$ and $\tau=t_{ini}$ of, e.g., the field-cooling process, whereas $V_{I/II}$ is defined by $T=T_{RT}$ and by a time $\tau=t_{spp}$. The latter is connected to the timescale on which very small thermally unstable AFM grains behave superparamagnetically. Assuming that the temperature dependence of K_{AFM} is $K_{AFM}(T)=K_{AFM}(0)(1-T/T_N)$ [42] with $T_N\approx 650$ K for IrMn [1,37,42], and using the experimentally determined values $K_{AFM}(T_{RT})=(5.5\pm0.5)\times10^5$ J/m^3 [37] and $\tau_0=1/(2.1\pm0.4)\times10^{-12}$ s^{-1} [42], the boundaries can be estimated for given observation temperatures and times.

For calculating the contributions of the grain classes, the integrals between the respective bounds [Fig. 1(a)] have to be determined. We define

$$p=\int_{V_{I/II}}^{V_{III/IV}}\varrho(V_{AFM})dV_{AFM} \quad (4)$$

as the percentage of grains contributing to the UDA and the RMA at all, i.e., all grains of classes II and III in relation to the number of all grains of the polycrystalline ensemble. Based on this, the contributions p_{II} and p_{III} of class II and III grains, respectively, are given as the weighted integrals between the respective bounds

$$p_{II}=\int_{V_{I/II}}^{V_{II/III}}\frac{\varrho(V_{AFM})}{p}\,dV_{AFM}, \quad (5)$$

$$p_{III}=\int_{V_{II/III}}^{V_{III/IV}}\frac{\varrho(V_{AFM})}{p}\,dV_{AFM}=1-p_{II}. \quad (6)$$

Knowing the parameters characterizing the distribution of grain sizes, p and $p_{III}=1-p_{II}$ can be expressed as functions of t_{AFM}, μ, σ, and the respective grain class boundaries by

$$\chi(V_{AFM},t_{AFM},\mu,\sigma)=\mathrm{erf}\left\{\frac{\ln\sqrt{V_{AFM}/\pi t_{AFM}}-\mu}{\sqrt{2\sigma^2}}\right\}, \quad (7)$$

where $(1+\chi)/2$, as the integral of the lognormal distribution, represents the proportion of grains that are smaller than or have the same size as V_{AFM}. p and p_{III} are given by

$$p = \{\chi(V_{\mathrm{III/IV}}, t_{\mathrm{AFM}}, \mu, \sigma) - \chi(V_{\mathrm{I/II}}, t_{\mathrm{AFM}}, \mu, \sigma)\}/2, \quad (8)$$

$$p_{\mathrm{III}} = \{\chi(V_{\mathrm{III/IV}}, t_{\mathrm{AFM}}, \mu, \sigma) - \chi(V_{\mathrm{II/III}}, t_{\mathrm{AFM}}, \mu, \sigma)\}/2p. \quad (9)$$

C. Thickness dependencies

Varying the layer thicknesses t_{AFM} and t_{FM} of an AFM/FM bilayer yields a very rich phenomenology with respect to the alteration of H_{EB} and H_{C}, due to the change in the AFM GVD as well as the coupling strength at the common interface [1,18,20,29]. Based on the intuitive SW approach introduced by Meiklejohn [2] and Meiklejohn and Bean [46] (see Ref. [18]), the absolute value of the EB shift and the coercive field are here assumed to be given by [1,18,20,47]

$$|H_{\mathrm{EB}}(t_{\mathrm{FM}}, t_{\mathrm{AFM}})| = \frac{J_{\mathrm{eff}}(t_{\mathrm{FM}}, t_{\mathrm{AFM}})}{\mu_0 M_{\mathrm{S}} t_{\mathrm{FM}}} p_{\mathrm{III}}(t_{\mathrm{AFM}}), \quad (10)$$

$$H_{\mathrm{C}}(t_{\mathrm{FM}}, t_{\mathrm{AFM}}) = \frac{J_{\mathrm{eff}}(t_{\mathrm{FM}}, t_{\mathrm{AFM}})}{\mu_0 M_{\mathrm{S}} t_{\mathrm{FM}}} p_{\mathrm{II}}(t_{\mathrm{AFM}}) + \frac{2K_{\mathrm{FM}}}{\mu_0 M_{\mathrm{S}}} \quad (11)$$

with H_{C} being shifted by an offset determined by the FM uniaxial anisotropy constant K_{FM} and saturation magnetization M_{S} [18]. The exchange bias shift is scaled by the product between the effective coupling constant $J_{\mathrm{eff}}(t_{\mathrm{FM}}, t_{\mathrm{AFM}})$ and the proportion $p_{\mathrm{III}}(t_{\mathrm{AFM}})$ of H_{EB}-mediating grains of class III, which should by definition [Eq. (6)] only depend on t_{AFM} [25,36]. Likewise, in the case of the coercivity, $H_{\mathrm{C}} - 2K_{\mathrm{FM}}/\mu_0 M_{\mathrm{S}}$ is scaled by the product of $J_{\mathrm{eff}}(t_{\mathrm{FM}}, t_{\mathrm{AFM}})$ and the proportion $p_{\mathrm{II}}(t_{\mathrm{AFM}})$ of class II grains mediating H_{C}, since the rotatable anisotropy is time dependent but of unidirectional nature [28]. The effective coupling constant is given by

$$J_{\mathrm{eff}}(t_{\mathrm{FM}}, t_{\mathrm{AFM}}) = J_{\mathrm{EB}}(t_{\mathrm{FM}}) p(t_{\mathrm{AFM}}) \quad (12)$$

assuming that $J_{\mathrm{EB}}(t_{\mathrm{FM}})$ is constant for all AFM grains ($J_{\mathrm{EB},i} = J_{\mathrm{EB}}\ \forall\, i$) and is already reduced due to, e.g., interface roughness, compensated moments, or stoichiometric gradients [1,18,21]. It is further supposed that the coupling itself is solely determined by the coupling interfaces and not the individual volumes of the AFM grains. $J_{\mathrm{eff}}(t_{\mathrm{FM}}, t_{\mathrm{AFM}})$ is proportional to $p(t_{\mathrm{AFM}})$ ensuring that the grain-class-specific exchange coupling constants $J_{\mathrm{II/III}} = J_{\mathrm{EB}} p p_{\mathrm{II/III}} = J_{\mathrm{EB}} A_{\mathrm{II/III}}/A$ are determined by the scaling of the microscopic exchange energy area density with the proportion of the area $A_{\mathrm{II/III}}$ accounted to the corresponding grain class with respect to the whole AFM/FM-interface area A [25,36].

D. Time-dependent Stoner-Wohlfarth ansatz

For numerical calculations of magnetization curves and the determination of $H_{\mathrm{EB/C}}^{\mathrm{SW}}(t_{\mathrm{FM}}, t_{\mathrm{AFM}})$ and for fitting model calculations $H_{\mathrm{EB/C}}^{\mathrm{SW}}(\varphi)$ to experimentally determined angular-resolved $H_{\mathrm{EB/C}}^{\mathrm{exp}}(\varphi)$, the extended time-dependent Stoner-Wohlfarth (SW) approach introduced in Refs. [26,28,36,48] will be utilized. During remagnetization, a uniform in-plane magnetized FM with magnetization $\vec{M}_{\mathrm{FM}}$ and saturation magnetization M_{S} is assumed to rotate coherently, where the azimuthal angle of $\vec{M}_{\mathrm{FM}}$ is given by β_{FM} [Fig. 1(b)]. Using the perfect delay convention [26,28,36,49], the time-dependent FM free-energy area density $E[\beta_{\mathrm{FM}}(t)]/A$ is sequentially minimized with respect to $\beta_{\mathrm{FM}}(t)$ for varying external magnetic field H.

$$E[\beta_{\mathrm{FM}}(t)]/A = e_{\mathrm{pot}} + e_{\mathrm{FUMA}} + e_{\mathrm{RMA}} + e_{\mathrm{UDA}} \quad (13)$$

is composed of the FM layer's potential energy density in the external magnetic field e_{pot}, its intrinsic uniaxial anisotropy e_{FUMA} (FUMA), and additional anisotropy terms e_{RMA} and e_{UDA} representing the interaction with superposed rotatable and fixed uncompensated AFM moments. The potential energy area density is given by

$$e_{\mathrm{pot}} = -\mu_0 H M_{\mathrm{S}} t_{\mathrm{FM}} \cos[\beta_{\mathrm{FM}}(t) - \varphi] \quad (14)$$

with μ_0 as the magnetic permeability in a vacuum and φ as the azimuthal angle of the external magnetic field with respect to an arbitrary reference frame [Fig. 1(b)]. The uniaxial anisotropy energy area density is given by

$$e_{\mathrm{FUMA}} = K_{\mathrm{FM}} t_{\mathrm{FM}} \sin^2[\beta_{\mathrm{FM}}(t) - \gamma_{\mathrm{FM}}] \quad (15)$$

with the energy density K_{FM} and the azimuthal angle γ_{FM} [Fig. 1(b)] defining the FM's anisotropy axis parallel to the external magnetic field applied during deposition [26,28]. The interaction of the uniform FM with AFM grains contributing to the RMA or the UDA is broken down to the interaction of the FM with the macroscopic uncompensated interface moments $\vec{M}_{\mathrm{C/EB}}^{\mathrm{II/III}} = \sum_i \vec{m}_{\mathrm{AFM},i}^{\mathrm{II/III}}$, with the azimuthal angles $\gamma_{\mathrm{C}}^{\mathrm{II}}$ and $\gamma_{\mathrm{EB}}^{\mathrm{III}}$ [Fig. 1(b)], as the superposition of the grain-averaged magnetic moments $\vec{m}_{\mathrm{AFM},i}^{\mathrm{II/III}}$ of classes II and III [28,36]. The anisotropy area densities representing the RMA and the UDA are given by [28,36]

$$e_{\mathrm{RMA}} = -J_{\mathrm{eff}} p_{\mathrm{II}} \cos\left[\beta_{\mathrm{FM}}(t) - \gamma_{\mathrm{C}}^{\mathrm{II}}\left(t, \tau_{\mathrm{C}}^{\mathrm{II}}\right)\right], \quad (16)$$

$$e_{\mathrm{UDA}} = -J_{\mathrm{eff}} p_{\mathrm{III}} \cos\left[\beta_{\mathrm{FM}}(t) - \gamma_{\mathrm{EB}}^{\mathrm{III}}\right] \quad (17)$$

with prefactors $J_{\mathrm{II/III}} = J_{\mathrm{eff}} p_{\mathrm{II/III}}$ [36] as in Eqs. (10) and (11). The time-dependent contribution of the dynamic RMA is represented by its azimuthal angle

$$\gamma_{\mathrm{C}}^{\mathrm{II}}\left(t, \tau_{\mathrm{C}}^{\mathrm{II}}\right) = \beta_{\mathrm{FM}}(t - \Delta t)\left(1 - \exp\left\{-\Delta t/\tau_{\mathrm{C}}^{\mathrm{II}}\right\}\right) + \gamma_{\mathrm{C}}^{\mathrm{II}}\left(t - \Delta t, \tau_{\mathrm{C}}^{\mathrm{II}}\right)\exp\left\{-\Delta t/\tau_{\mathrm{C}}^{\mathrm{II}}\right\} \quad (18)$$

with the average relaxation time

$$\tau_{\mathrm{C}}^{\mathrm{II}} = \frac{\int_{V_{\mathrm{I/II}}}^{V_{\mathrm{II/III}}} \tau_{\mathrm{AFM}}(V_{\mathrm{AFM}}) \varrho(V_{\mathrm{AFM}})\, dV_{\mathrm{AFM}}}{\int_{V_{\mathrm{I/II}}}^{V_{\mathrm{II/III}}} \varrho(V_{\mathrm{AFM}})\, dV_{\mathrm{AFM}}} \quad (19)$$

of all rotatable grains of class II [27,36]. The dynamic realignment of the RMA is visualized in Fig. 1(c) showing that for each step during the remagnetization of the FM, for which $\beta_{\mathrm{FM}}(t)$ is determined, $\gamma_{\mathrm{C}}^{\mathrm{II}}(t, \tau_{\mathrm{C}}^{\mathrm{II}})$ is derived from the history of the FM and the RMA at $t - \Delta t$ [26,28,36].

Additionally, to consider a possible offset of $H_{\mathrm{EB}}(\varphi)$ due to the measurement procedure, which is not related to training effects, an additional magnetic anisotropy term $e_{\mathrm{add}} = -J_{\mathrm{add}} \cos[\beta_{\mathrm{FM}}(t) - \varphi]$ is added to Eq. (13) [28]. This additional term incorporates the interaction of the FM with AFM

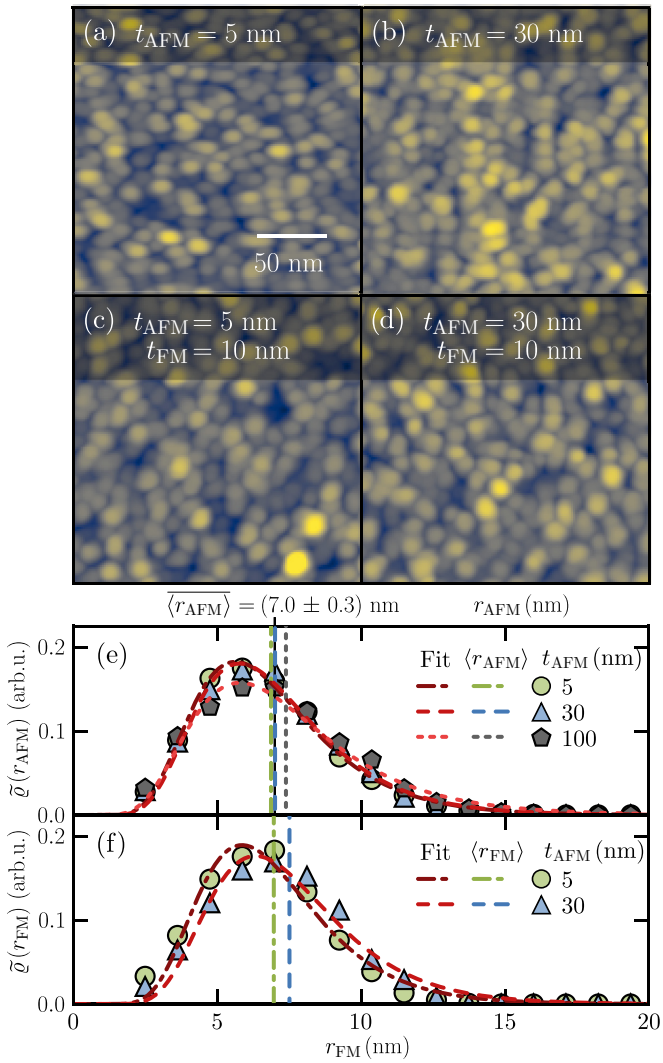

FIG. 2. Atomic force microscopy images of the IrMn surface for (a) $t_{AFM} = 5$ and (b) 30 nm and of the CoFe layer for $t_{FM} = 10$ nm deposited on IrMn for (c) $t_{AFM} = 5$ and (d) 30 nm. Distributions (e) $\tilde{\varrho}(r_{AFM})$ of the grain radius r_{AFM} for $t_{AFM} = 5$, 30, and 100 nm with corresponding lognormal fits and distributions (f) $\tilde{\varrho}(r_{FM})$ of r_{FM} for $t_{AFM} = 5$ and 30 nm.

grains which align in a direction parallel to the applied external magnetic field, determined by the additional effective coupling constant J_{add}. Since in the experiment φ is varied successively and not randomly, AFM grains which are in the vicinity of the grain class boundary between classes II and III having relaxation times larger than or similar to t_{Hys} do not contribute on the timescale of the hysteresis to the coercive field, but to the exchange bias shift on the timescale of the angular-resolved measurement.

In order to quantitatively extract model parameters from $H_{EB/C}^{exp}(\varphi)$, model calculations $H_{EB/C}^{SW}(\varphi)$ are fitted to the experimentally determined dependencies (see the Appendix, Table III, fit scenario SW). For this, hysteresis loops are simulated by sequentially minimizing Eq. (13) for varying measurement angle φ. As for the experimental case, the EB shift $H_{EB}^{SW}(\varphi)$ and the coercive field $H_{C}^{SW}(\varphi)$ are derived from the zero crossings of the calculated angle-specific hysteresis loops. The procedure is described in more detail in Ref. [26] alongside a description of how the optimal parameters' uncertainties are estimated.

IV. RESULTS AND DISCUSSION

A. Surface topography

Figures 2(a) and 2(b) show the surface topography of the IrMn layer for $t_{AFM} = 5$ and 30 nm, measured by atomic force microscopy. Figures 2(c) and 2(d) show the AFM layers of the same thicknesses covered by 10-nm CoFe. For all t_{AFM}, the IrMn and the CoFe layer exhibit a similar polycrystalline structure with almost circular base areas, indicating columnar grain growth with cylindrically shaped grains [26]. The root-mean-square surface roughness of the IrMn layer showed for $5\ \text{nm} \leqslant t_{AFM} \leqslant 50$ nm no significant trend, and the average value could be determined to be (0.29 ± 0.04) nm, whereas for $t_{AFM} = 100$ nm it was determined to be (0.48 ± 0.04) nm. In the case of the CoFe layer, the root-mean-square surface roughness was determined to be (0.41 ± 0.11) nm.

Histograms displaying the distribution $\tilde{\varrho}(r_{AFM})$ of AFM grain radii determined with the watershed algorithm are depicted with lognormal fits in Fig. 2(e) exemplarily for $t_{AFM} =$ 5, 30, and 100 nm. $\tilde{\varrho}(r_{AFM})$ does not change significantly for varying t_{AFM}. We conclude that the expectation value $\langle r_{AFM} \rangle$ of the AFM grain radius is constant for the investigated thicknesses and the average value could be determined to be $\overline{\langle r_{AFM} \rangle} = (7.0 \pm 0.3)$ nm. In combination with Ref. [26], this validates the assumption of a homogeneous columnar grain growth for the used deposition parameters enabling a linear scaling of the individual AFM grain volumes $V_{AFM} = \pi {r_{AFM}}^2 t_{AFM}$ with t_{AFM}.

In Fig. 2(f), the distribution $\tilde{\varrho}(r_{FM})$ of FM grain radii in the case of $t_{FM} = 10$ nm at $t_{AFM} = 5$ and 30 nm reveals that the polycrystalline CoFe layer inherits the distribution of grain interfaces from the underlying IrMn layer with a trend towards larger $\langle r_{FM} \rangle$ for increasing t_{AFM}.

B. Magnetic properties

In the following description of the determined thickness-dependent magnetic properties, a series of fit procedures are performed based on the equations introduced in Sec. III. A detailed overview of the different fit scenarios is given in the Appendix in Table III.

1. Ferromagnetic thickness dependence

Experimentally determined $|H_{EB}^{exp}(t_{FM})|$ and $H_{C}^{exp}(t_{FM})$ are depicted in Figs. 3(a)–3(d) for $t_{AFM} = 5$ and 30 nm. The inverse proportionality is obvious as well as the offset for H_C, with the coercivity not changing significantly from $t_{FM} = 20$ nm for both values of t_{AFM}. While for $t_{AFM} = 5$ nm, H_C decreases until $t_{FM} = 30$ nm down to (5.5 ± 0.9) kA/m, for $t_{AFM} = 30$ nm a reduction to (3.1 ± 0.7) kA/m is observable. With Eq. (11), this suggests an increase in K_{FM} or a reduction in M_S for small t_{AFM}.

Fitting simulated $H_{EB/C}^{SW}(\varphi)$ to experimentally determined $H_{EB/C}^{exp}(\varphi)$ (Table III, fit scenario SW) for varying t_{FM} at $t_{AFM} = 5$ and 30 nm allowed for the determination of model

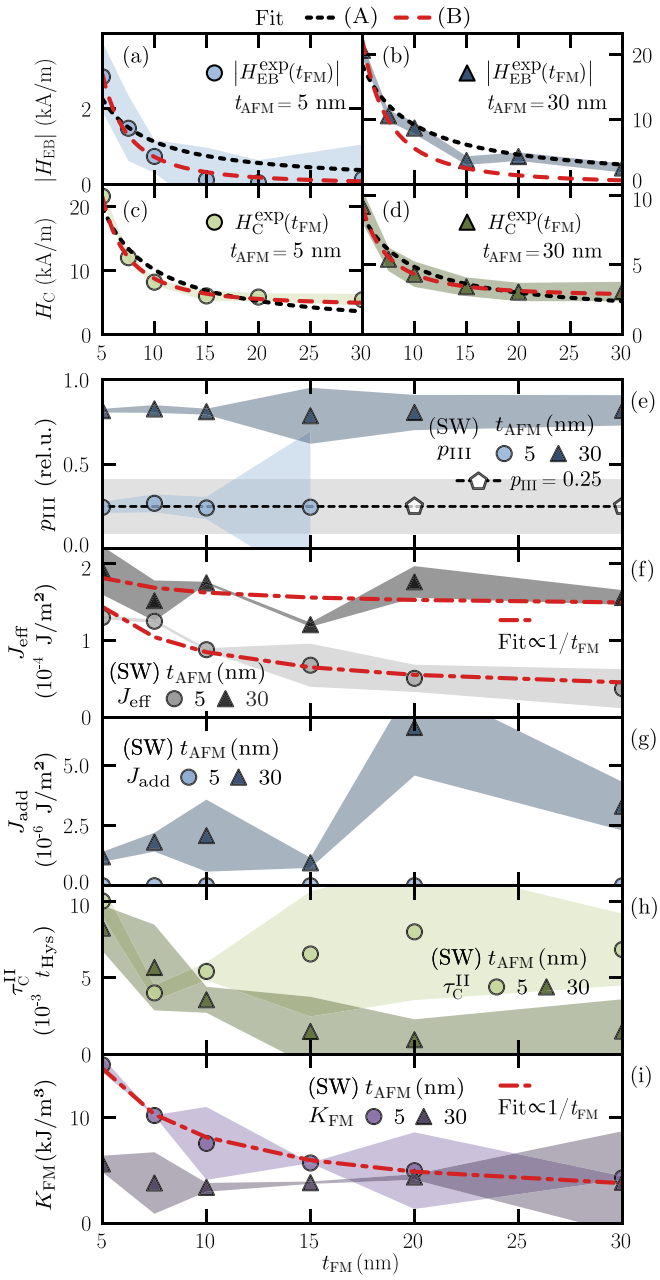

FIG. 3. t_{FM}-dependent (a) and (b) $|H_{EB}^{exp}|$ and (c) and (d) H_C^{exp} as well as parameters (e) p_{III}, (f) J_{eff}, (g) J_{add}, (h) τ_C^{II}, and (i) K_{FM} obtained by fitting $H_{EB/C}^{SW}(\varphi)$ to $H_{EB/C}^{exp}(\varphi)$ (Table III, fit scenario SW) for $t_{AFM}=5$ and 30 nm. Fits in (a) and (b) are based on Eqs. (10) and (11), proportional to $1/t_{FM}$ with fit parameters $J_{II/III}=J_{eff}p_{II/III}$ in the case of fit scenario A and proportional to $1/t_{FM}^2$ in the case of fit scenario B with $J_{II/III}(t_{FM})=j_{II/III}/t_{FM}$ (Table III, fit scenarios A and B). Here, rel., relative.

parameters. Angles γ_{FM} and γ_{EB}^{III} were not fixed but showed no significant trend. The saturation magnetization $M_S=(1527\pm 25)$ kA/m of the CoFe layer in contact with the AFM was determined for $t_{FM}=10$ nm and both values of t_{AFM} by utilizing a vector network analyzer ferromagnetic resonance spectrometer. The extracted optimum parameters are displayed in Figs. 3(e)–3(i) and are discussed in the following.

p_{III}. The proportion p_{III} of class III grains [Fig. 3(e)] shows no significant dependence on t_{FM} for $t_{AFM}=30$ nm, staying constant at $\langle p_{III}\rangle=(0.81\pm 0.08)$. For $t_{AFM}=5$ nm and $t_{FM}\leqslant 15$ nm, $\langle p_{III}\rangle=(0.25\pm 0.16)$, but for $t_{FM}>15$ nm the fit procedure results in a suppression of p_{III} accompanied by a large uncertainty due to the rising difficulty of extracting EB-related parameters for increasing t_{FM}. Since a larger FM layer thickness should not result in a change in p_{III}, it has been set constant to 0.25 at $t_{FM}=20$ and 30 nm for $t_{AFM}=5$ nm. The scaling of grain number percentages of class II or III with t_{AFM} reproduces the expectation of a reduced p_{III} at small t_{AFM}.

J_{eff}. The effective coupling constant J_{eff} [Fig. 3(f)] decreases for increasing t_{FM} for both values of t_{AFM}. As with $|H_{EB}|\propto J_{eff}/t_{FM}$, the satisfying fit $\propto 1/t_{FM}$ with respect to $J_{eff}(t_{FM})$ suggests that $J_{EB}\propto 1/t_{FM}$ by considering Eq. (12). This is more apparent for $t_{AFM}=5$ nm with a reduction in J_{eff} to $\approx$45%, whereas for $t_{AFM}=30$ nm J_{eff} reduces to $\approx$82%. Hence the AFM layer thickness has an impact on the t_{FM} dependence of J_{eff}. This is qualitatively understandable since a stronger contribution of class II grains is connected to a larger grain-interface-to-grain-volume ratio and a reduction in K_{AFM} at smaller grain sizes [37]. For smaller grain sizes, where $\Delta E_{AFM}=K_{AFM}V_{AFM}$ starts to lose its validity, this influences crucially how smaller grains interact with the FM [25,27,37].

J_{add}. The additional effective coupling constant J_{add} [Fig. 3(g)] exhibits no dependence on t_{FM} but a trend to be larger for increasing t_{AFM}.

τ_C^{II}. The average relaxation time τ_C^{II} in units of t_{Hys} [Fig. 3(h)] exhibits an overall reduction with increasing t_{FM} for both values of t_{AFM}, whereas for $t_{AFM}=30$ nm an antiproportional dependence on t_{FM} similar to $H_C(t_{FM})$ in Fig. 3(d) is observable. In the case of $t_{AFM}=5$ nm, no significant trend is observable for $t_{FM}\geqslant 7.5$ nm. The alteration of τ_C^{II} with t_{FM} for fixed t_{AFM} can only be explained by a t_{FM}-dependent variation of the interaction between the FM and the polycrystalline AFM caused by a differing magnetization reversal for different values of t_{FM} [36,50].

K_{FM}. The anisotropy constant K_{FM} [Fig. 3(i)] exhibits no significant trend for $t_{AFM}=30$ nm. In contrast, for $t_{AFM}=5$ nm an antiproportional dependence on t_{FM} is observable as for J_{eff} in Fig. 3(f) and H_C in Fig. 3(c) approaching $K_{FM}(t_{AFM}=30$ nm) for large t_{FM}. The intrinsic uniaxial anisotropy is probably overestimated by the fit (Table III, fit scenario SW) and is connected to the increase in H_C for small t_{FM}. This entanglement of the FUMA with the RMA is further emphasized by the fit $\propto 1/t_{FM}$ depicted in Fig. 3(i), which is in satisfying agreement with $K_{FM}(t_{FM})$ for $t_{AFM}=5$ nm.

Now our aim is the extraction of parameters by fitting $|H_{EB}(t_{FM})|$ and $H_C(t_{FM})$ given by Eqs. (10) and (11) to $|H_{EB}^{exp}(t_{FM})|$ and $H_C^{exp}(t_{FM})$ as displayed in Figs. 3(a)–3(d) (Table III, fit scenarios A and B). In the case of fit scenario A, $J_{II}=J_{eff}p_{II}$ and $J_{III}=J_{eff}p_{III}$ have been used as fit parameters scaling the contribution of the UDA and RMA, respectively. Furthermore, the most important result, relating to the determined model parameters shown in Figs. 3(e)–3(i), is the observed additional antiproportional t_{FM} dependence of the effective coupling constant J_{eff}. Considering this, relations based on Eqs. (10) and (11) are fitted to $|H_{EB}^{exp}(t_{FM})|$ and $H_C^{exp}(t_{FM})$ with $J_{II/III}(t_{FM})=j_{II/III}/t_{FM}$ and $j_{II/III}$ as the

TABLE I. Parameters obtained for the prototypical bilayer system $Ir_{17}Mn_{83}(t_{AFM})/Co_{70}Fe_{30}(t_{FM})$ by fitting relations based on Eqs. (10) and (11) to $|H_{EB}^{exp}(t_{FM})|$ and $H_C^{exp}(t_{FM})$ [Figs. 3(a)–3(d)] proportional to $1/t_{FM}$ (fit scenario A) with fit parameters $J_{II/III} = J_{eff}\, p_{II/III}$ or with relations proportional to $1/{t_{FM}}^2$ (fit scenario B) with $J_{II/III}(t_{FM}) = j_{II/III}/t_{FM}$ (Table III, fit scenarios A and B); parameters [Figs. 4(b), 4(c), and 4(f)] determined by fitting $H_{EB/C}^{SW}(\varphi)$ to $H_{EB/C}^{exp}(\varphi)$ (Table III, fit scenario SW) for $t_{AFM} = 5$ and 30 nm with $t_{FM} = 10$ nm; and parameters obtained by fitting Eqs. (10) and (11) to $|H_{EB}^{exp}(t_{AFM})|$ and $H_C^{exp}(t_{AFM})$ as displayed in Fig. 4(a) (Table III, fit scenario C). Furthermore, optimum parameters are displayed extracted by fitting Eq. (12) to $J_{eff}(t_{AFM})$ (from fit scenario SW) in Fig. 4(c) (Table III, fit scenario J), and finally, p_{III}^{max} is presented obtained by fitting Eq. (9), linked to Eq. (8), to $p_{III}(t_{AFM})$ (from fit scenario SW) in Fig. 4(b) (Table III, fit scenario P).

		$t_{FM} = 10$ nm	$t_{AFM} = 5, 30$ nm		$t_{FM} = 10$ nm		
Parameter	Thickness	SW	A	B	C	C	SW, J and P
J_{EB} (10^{-5} J/m^2)	$t_{FM} = 10$ nm				18.91 ± 12.58	27.66 ± 8.89	21.74 ± 0.61
J_{II} (10^{-5} J/m^2)	$t_{AFM} = 5$ nm	7.35 ± 3.67	18.75 ± 2.50	8.13 ± 0.25			
	$t_{AFM} = 30$ nm	3.80 ± 6.65	7.05 ± 0.90	3.05 ± 0.08			
J_{III} (10^{-5} J/m^2)	$t_{AFM} = 5$ nm	2.78 ± 2.24	2.17 ± 0.35	1.40 ± 0.06			
	$t_{AFM} = 30$ nm	18.18 ± 8.92	17.62 ± 1.20	10.64 ± 0.97			
K_{FM} (kJ/m^3)	$t_{FM} = 10$ nm					1.21 ± 0.51	
	$t_{AFM} = 5$ nm	10.68 ± 5.74	0.40 ± 1.41	4.37 ± 0.23			
	$t_{AFM} = 30$ nm	3.80 ± 4.37	1.14 ± 0.50	2.64 ± 0.07			
μ (nm)					1.12 ± 0.08	1.08 ± 7.90	1.08 ± 1.05
σ (nm)					0.15 ± 0.01	0.17 ± 0.07	0.09 ± 0.56
$\langle r_{AFM} \rangle$ (nm)					3.09 ± 0.25	2.97 ± 2.34	2.94 ± 3.23
SD (nm)	$t_{FM} = 10$ nm				0.47 ± 0.24	0.50 ± 6.24	0.25 ± 0.98
$V_{I/II}$ (nm^3)					8 ± 20	112 ± 177	130 ± 305
$V_{II/III}$ (nm^3)					217 ± 35	255 ± 50	
$V_{III/IV}$ (nm^3)					2589 ± 350	1717 ± 271	2242 ± 18
p_{III}^{max}					0.96 ± 0.38	0.70 ± 0.19	0.85 ± 0.03

proportionality factor of the respective effective coupling constant in the case of fit scenario B. The obtained parameters are given in Table I for the two investigated t_{AFM} values, $t_{AFM} = 5$ and 30 nm, in comparison to the parameters obtained by fitting model calculations based on the time-dependent SW ansatz [Eq. (13)] for $t_{FM} = 10$ nm, presented in Figs. 3(e)–3(i).

Comparing the effective coupling constants J_{II} and J_{III} obtained using the SW ansatz with the parameters determined from fit scenario A or B it can be seen that J_{II} is overestimated by fit scenario A but reproduced by fit scenario B. In contrast, for J_{III} it is vice versa, with fit scenario B underestimating J_{III}, especially in the case of $t_{AFM} = 30$ nm. Parameters J_{II} and J_{III} obtained by fit scenario B are in all cases in agreement with the parameters determined via the SW ansatz within their ranges of uncertainties. The average absolute deviation between the data points and fit scenario B is always smaller than 10% of the deviation between the data points and fit scenario A, except for J_{III} and $t_{AFM} = 30$ nm. This is in good agreement with the antiproportional t_{FM} dependence of J_{eff} for $t_{AFM} = 5$ nm [Fig. 3(f)]. As stated above, it is expected that the extended SW ansatz overestimates the intrinsic FUMA of the FM due to an entanglement with the RMA. Hence the anisotropy constant K_{FM} determined by both fit scenario A and fit scenario B and for both values of t_{AFM} is smaller than the values determined by the fit based on Eq. (13).

Equations (10) and (11) are therefore in good agreement with the time-dependent SW approach when an antiproportional dependence of J_{eff} on t_{FM} [Fig. 3(f)] is introduced. The latter additionally depends on t_{AFM}, and investigations presented in the literature further suggest that in general $H_C + \text{const} \propto 1/{t_{FM}}^n$ and $H_{EB} \propto 1/{t_{FM}}^m$ with $1 \leqslant n, m \leqslant 2$ [33]. Although the $1/t_{FM}$ dependence of the exchange bias shift and the coercivity has been tested and validated for a variety of systems [1,20,51,52], deviations from this with $n, m > 1$ [33,53,54] should be considered depending on measurement conditions as well as the microstructure of the system [33].

2. *Antiferromagnetic thickness dependence*

$|H_{EB}^{exp}(t_{AFM})|$ and $H_C^{exp}(t_{AFM})$ for $t_{FM} = 10$ nm are displayed in Fig. 4(a). The commonly observed dependence [1,20,29,51] is reproduced, where a significant EB shift starts to be observable for $t_{AFM} \geqslant 5$ nm, increasing up to $t_{AFM} = 12.5$ nm. The EB shift stays constant at about (9.3 ± 1.2) kA/m as the average absolute value for $t_{AFM} \leqslant 12.5$ nm. The coercivity shows a significant increase for 2.5 nm $< t_{AFM} <$ 5 nm over $\langle H_C^{exp} \rangle = (1.7 \pm 1.2)$ kA/m (average value for $t_{AFM} \leqslant 2.5$ nm representing the coercive field of the sole FM layer) and exhibits a maximum value of $H_C^{exp} = (12.4 + 1.1)$ kA/m at $t_{AFM} = 7.5$ nm. At this thickness, $|H_{EB}^{exp}(t_{AFM})|$ has the largest slope. For larger t_{AFM} the coercivity decreases, as the EB shift reaches its plateau, until it does not change significantly and stays constant at $\langle H_C^{exp} \rangle = (5.0 \pm 1.2)$ kA/m for $t_{AFM} \geqslant 30$ nm.

Also here, model calculations $H_{EB/C}^{SW}(\varphi)$ based on Eq. (13) are fitted to $H_{EB/C}^{exp}(\varphi)$ (Table III, fit scenario SW) as functions of t_{AFM} for $t_{FM} = 10$ nm with $M_S = (1527 \pm 25)$ kA/m and angles $\gamma_{FM} \neq \gamma_{EB}^{III} \neq 0$, with the latter exhibiting no significant dependence. Optimum parameters extracted for $t_{AFM} \geqslant 5$ nm are shown in Figs. 4(b)–4(f) and are discussed in the following.

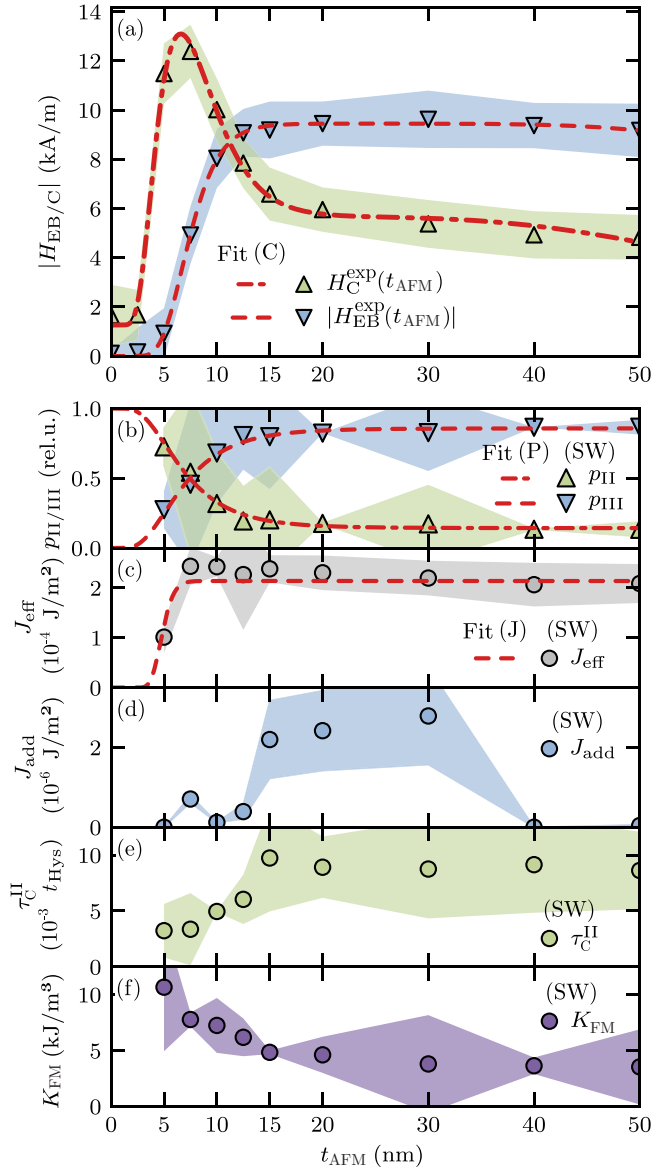

FIG. 4. t_{AFM}-dependent (a) $|H_{EB}^{exp}|$ and H_C^{exp} as well as parameters (b) $p_{III} = 1 - p_{II}$, (c) J_{eff}, (d) J_{add}, (e) τ_C^{II}, and (f) K_{FM} obtained by fitting $H_{EB/C}^{SW}(\varphi)$ to $H_{EB/C}^{exp}(\varphi)$ (Table III, fit scenario SW) for $t_{FM} =$ 10 nm. The fit scenarios C, P, and J in (a)–(c) are based on Eqs. (10), (11), (8), (9), and (12) (Table III, fit scenarios C, P, and J).

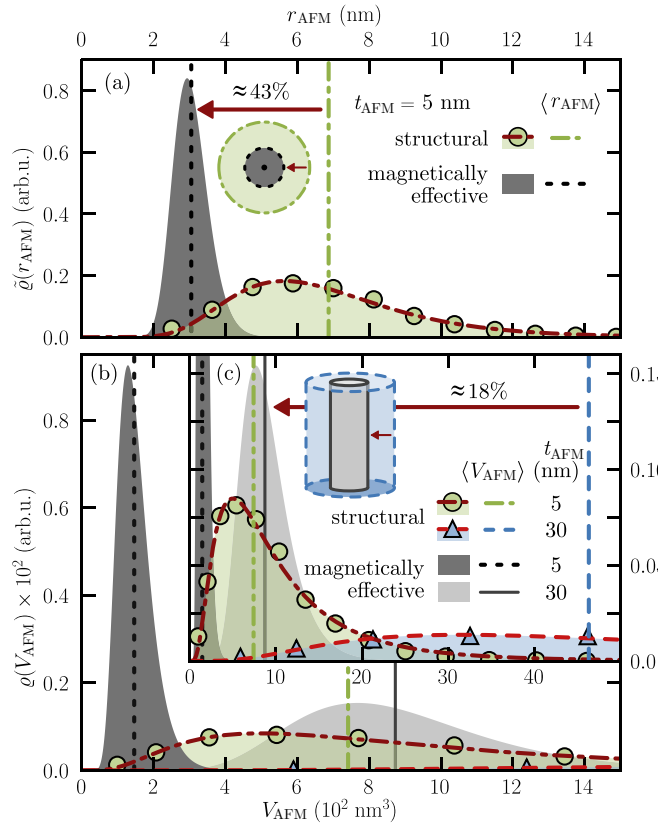

FIG. 5. (a) Comparison of the structural ($t_{AFM} = 5$ nm [Fig. 2(e)]) and magnetically effective AFM grain radius distribution $\tilde{\varrho}(r_{AFM})$ based on the experimentally performed grain size analysis by atomic force microscopy and the extracted parameters μ and σ given in Table I (Table III, fit scenario C), respectively. (b) and (c) Structural and magnetically effective AFM GVD $\varrho(V_{AFM})$ have been subsequently derived by use of Eq. (2) for $t_{AFM} = 5$ and 30 nm. Notice that (b) and (c) display the same data but with different axis limits. The expectation values of the AFM grain radius and volume, $\langle r_{AFM} \rangle$ and $\langle V_{AFM} \rangle$, are depicted, and lognormal fits are given with respect to the structural AFM grain radius and volume distributions.

p_{III}. The percentages $p_{III}(t_{AFM}) = 1 - p_{II}(t_{AFM})$ are given in Fig. 4(b) with p_{III} increasing with increasing t_{AFM} as $|H_{EB}^{exp}(t_{AFM})|$ in Fig. 4(a), reaching a constant value $\langle p_{III} \rangle = (0.8 \pm 0.2)$ when the average for $t_{AFM} \geqslant 12.5$ nm, much like the EB shift as a function of t_{AFM}. This implies a gradual shift of the AFM GVD to larger AFM grain volumes. As larger AFM grains are more probable in the thicker polycrystalline AFM layers, the proportion of grains accounted to class III increases while the proportion of grains accounted to class II decreases. Since p_{II} and p_{III} are defined as the percentages of grains accounted to the respective grain classes, p_{II} will approach 1 for small t_{AFM}. Displayed in Fig. 4(b) are fits using Eq. (9), extended by the multiplicative factor p_{III}^{max}, to $p_{III}(t_{AFM}) = 1 - p_{II}(t_{AFM})$ (Table III, fit scenario P), considering that p_{III} does not approach exactly 1 for increasing t_{AFM}. The nonzero percentage of grains belonging to class II at large t_{AFM} is caused by a nonideal interrupted columnar growth, where a certain percentage of grains will not grow over the complete thickness of the layer, resulting in effectively smaller AFM grains in contact with the FM. Consequently, there will be always a finite nonzero amount of AFM grains that can be associated with class II for increasing t_{AFM}.

J_{eff}. The effective coupling constant [Fig. 4(c)], as defined in Eq. (12), increases and stays constant within the margin of uncertainty at $\langle J_{eff} \rangle = (2.3 \pm 0.6) \times 10^{-4}$ J/m² for $t_{AFM} \geqslant 7.5$ nm, with a decreasing tendency for increasing t_{AFM}. Assuming a constant microscopic coupling constant J_{EB}, this suggests that at $t_{AFM} = 7.5$ nm, most of the AFM grains belong to class II or III. For increasing t_{AFM} the percentage of class IV grains will increase accompanied by a decrease in $p(t_{AFM})$. Equation (12), describing $J_{eff}(t_{AFM})$ linked to $p(t_{AFM})$ defined by Eq. (8), is fitted to the values presented in Fig. 4(c) (Table III, fit scenario J), yielding the microscopic coupling constant $J_{EB} = (2.17 \pm 0.06) \times 10^{-4}$ J/m².

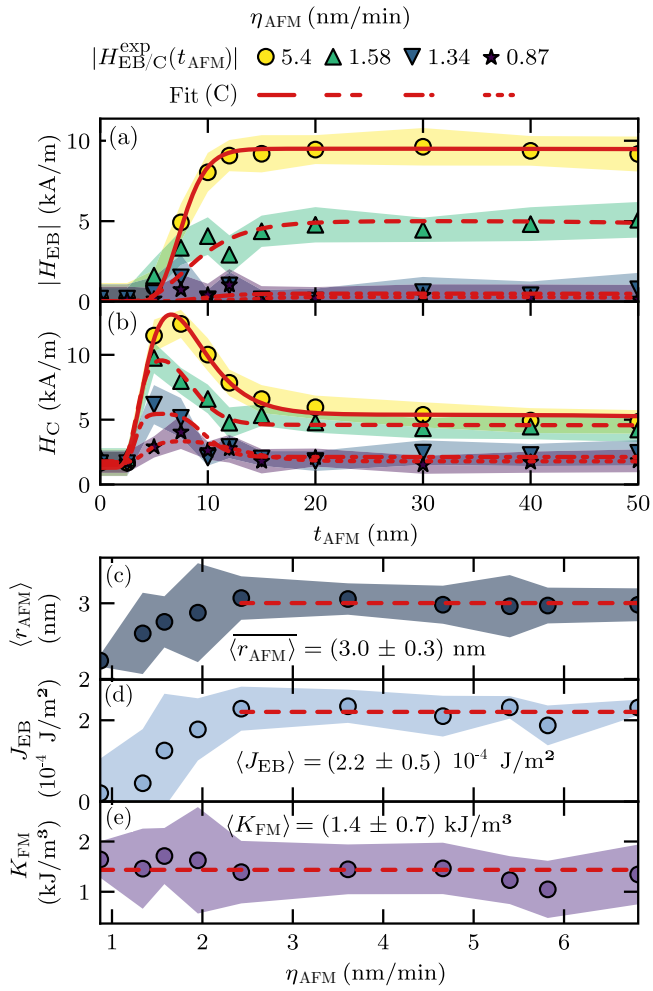

FIG. 6. (a) $|H_{\mathrm{EB}}^{\mathrm{exp}}(t_{\mathrm{AFM}})|$ and (b) $H_{\mathrm{C}}^{\mathrm{exp}}(t_{\mathrm{AFM}})$ for different deposition rates η_{AFM} of the AFM layer with corresponding fits using Eqs. (10) and (11) (Table III, fit scenario C). η_{AFM}-dependent (c) $\langle r_{\mathrm{AFM}} \rangle$, (d) J_{EB}, and (e) K_{FM} as averages of parameters obtained from fitting Eqs. (10) and (11) to t_{AFM}-dependent relations in (a) and (b). Average values in the η_{AFM} intervals indicated by dashed lines are additionally displayed.

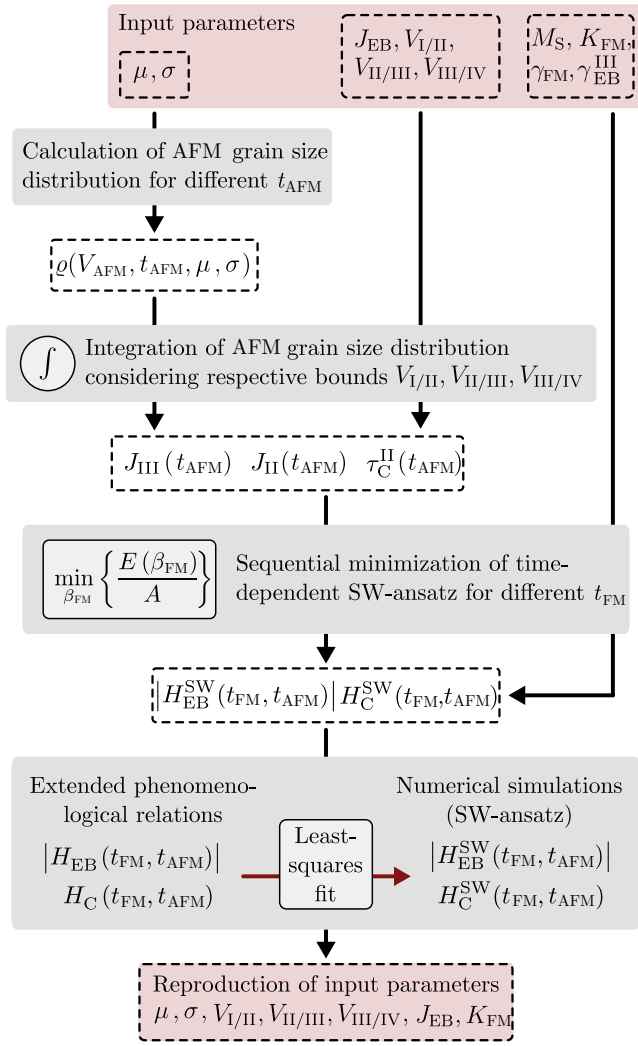

FIG. 7. Flowchart describing the cross-check's individual steps comparing simulated $|H_{\mathrm{EB}}^{\mathrm{SW}}(t_{\mathrm{FM}}, t_{\mathrm{AFM}})|$ and $H_{\mathrm{C}}^{\mathrm{SW}}(t_{\mathrm{FM}}, t_{\mathrm{AFM}})$, using the time-dependent SW ansatz [Eq. (13)], with the extended phenomenological relations $|H_{\mathrm{EB}}(t_{\mathrm{FM}}, t_{\mathrm{AFM}})|$ and $H_{\mathrm{C}}(t_{\mathrm{FM}}, t_{\mathrm{AFM}})$ defined by Eqs. (10) and (11). It is aimed at reproducing the input parameters by fitting the relations to the simulated values (Table III, scenario CC) in order to check for the validity of Eqs. (10) and (11) in the context of the time-dependent SW ansatz on the basis of calculated AFM GVDs.

J_{add}. The additional effective coupling constant J_{add} [Fig. 4(d)] shows a significant enhancement between $t_{\mathrm{AFM}} = 15$ nm and $t_{\mathrm{AFM}} = 30$ nm. This occurs in the thickness regime where the decrease in $H_{\mathrm{C}}^{\mathrm{exp}}$ with t_{AFM} slows down to a constant value. J_{add} is therefore connected with AFM grains in the vicinity of the grain class boundary between classes II and III.

$\tau_{\mathrm{C}}^{\mathrm{II}}$. In Fig. 4(e), the average relaxation time $\tau_{\mathrm{C}}^{\mathrm{II}}$ of grains associated with class II at room temperature is displayed in units of t_{Hys}. It increases with increasing t_{AFM} and reaches a plateau with an average value $\langle \tau_{\mathrm{C}}^{\mathrm{II}} \rangle = (9 \pm 4) \times 10^{-3}\ t_{\mathrm{Hys}}$ for $t_{\mathrm{AFM}} \geqslant 15$ nm. With the average hysteresis duration $t_{\mathrm{Hys}} \approx 44$ s of the angular-resolved measurements, this gives an average relaxation time of H_{C}-mediating grains of (390 ± 170) ms. The increase in $\tau_{\mathrm{C}}^{\mathrm{II}}$ with t_{AFM} and its saturation for larger t_{AFM} are in agreement with the general description of polycrystalline EB systems as well as the definition given in Eq. (19) [28]. As the averaging of τ_{AFM} is performed within the boundaries of class II [Eq. (19)], $\tau_{\mathrm{C}}^{\mathrm{II}}$ should increase for increasing t_{AFM} until the expectation value of the AFM GVD passes the class boundary $V_{\mathrm{II/III}}$. From there, $\tau_{\mathrm{C}}^{\mathrm{II}}$ will not increase further.

K_{FM}. The anisotropy constant K_{FM} [Fig. 4(f)] decreases from $K_{\mathrm{FM}} = (11 \pm 6)$ kJ/m^3 and stays constant at $\langle K_{\mathrm{FM}} \rangle = (4 \pm 4)$ kJ/m^3 within the range of uncertainty for $t_{\mathrm{AFM}} \geqslant 30$ nm. As the course of $K_{\mathrm{FM}}(t_{\mathrm{AFM}})$ is comparable to that of $H_{\mathrm{C}}^{\mathrm{exp}}(t_{\mathrm{AFM}})$ in Fig. 4(a), and likewise to the t_{FM} dependence of K_{FM} displayed in Fig. 3(i), the observable increase for small $t_{\mathrm{AFM}} \geqslant 5$ nm is linked to an entanglement of the FM's intrinsic FUMA with the RMA [36].

The fits in Figs. 4(b) and 4(c) with respect to $p_{\mathrm{III}}(t_{\mathrm{AFM}}) = 1 - p_{\mathrm{II}}(t_{\mathrm{AFM}})$ and $J_{\mathrm{eff}}(t_{\mathrm{AFM}})$ (Table III, fit scenarios P and

TABLE II. Input parameters for calculated AFM grain size distributions as well as simulated $|H_{EB}^{SW}(t_{FM}, t_{AFM})|$ and $H_C^{SW}(t_{FM}, t_{AFM})$ displayed in Fig. 8, representing the average values of the respective parameters given in Table I obtained from fitting Eqs. (10) and (11) to $|H_{EB}^{exp}(t_{AFM})|$ and $H_C^{exp}(t_{AFM})$ (Table III, fit scenario C) as displayed in Fig. 4(a). Optimum parameters obtained from fitting Eqs. (10) and (11) to simulated $|H_{EB}^{SW}(t_{FM}, t_{AFM})|$ and $H_C^{SW}(t_{FM}, t_{AFM})$ are given, reproducing the input parameters of the simulations using the time-dependent SW ansatz based on Eq. (13) (Table III, fit scenario CC).

		$t_{AFM} = 10$ nm	$t_{FM} = 10$ nm	
Parameter	Input	AC	CC	CC
J_{EB} (10^{-5} J/m^2)	23.29		23.35 ± 14.53	23.17 ± 1.65
J_{II} (10^{-5} J/m^2)	6.70	5.97 ± 0.06		
J_{III} (10^{-5} J/m^2)	16.59	16.80 ± 0.04		
K_{FM} (kJ/m^3)	1.21	0.34 ± 0.07		1.21 ± 0.32
μ (nm)	1.10		1.10 ± 0.89	1.10 ± 0.58
σ (nm)	0.16		0.16 ± 0.01	0.16 ± 0.03
$\langle r_{AFM} \rangle$ (nm)	3.03		3.05 ± 2.71	3.05 ± 1.78
SD (nm)	0.48		0.49 ± 0.21	0.48 ± 0.52
$V_{I/II}$ (nm^3)	60		60 ± 14	60 ± 70
$V_{II/III}$ (nm^3)	236		237 ± 422	235 ± 274
$V_{III/IV}$ (nm^3)	2153		2142 ± 381	2142 ± 160

J), respectively, validate Eqs. (8) and (9) describing the t_{AFM} dependence of p and p_{III}. Consequently, by incorporating these equations together with Eq. (12) into Eqs. (10) and (11), relations $|H_{EB}(t_{AFM})|$ and $H_C(t_{AFM})$ can be fitted to the experimentally determined $|H_{EB}^{exp}(t_{AFM})|$ and $H_C^{exp}(t_{AFM})$ as displayed in Fig. 4(a) (Table III, fit scenario C). As Eqs. (8) and (9) additionally depend on the grain class boundaries $V_{I/II}$, $V_{II/III}$, and $V_{III/IV}$ and on the parameters μ and σ describing the distribution of AFM grain radii r_{AFM}, these parameters connect the t_{AFM}-dependent relations of the EB shift and the coercive field with the polycrystalline AFM GVD and the measurement conditions. The determined fit parameters are presented in Table I.

Although the fit to $|H_{EB}^{exp}(t_{AFM})|$ in Fig. 4(a) yields $J_{EB} = (1.9 \pm 1.3) \times 10^{-4}$ J/m^2 and the fit to $H_C^{exp}(t_{AFM})$ gives $J_{EB} = (2.8 \pm 0.9) \times 10^{-4}$ J/m^2 displaying rather large uncertainties, both values agree with $J_{EB} = (2.17 \pm 0.06) \times 10^{-4}$ J/m^2, obtained from fitting $J_{eff}(t_{AFM})$ in Fig. 4(c) (Table III, fit scenario J), as estimates for the microscopic coupling constant J_{EB}. $K_{FM} = (1.2 \pm 0.5)$ kJ/m^3 determined by fitting Eq. (11) to $H_C^{exp}(t_{AFM})$ is significantly smaller than the values determined by fitting model calculations based on the SW ansatz (fit scenario SW) and by the t_{FM}-dependent fit (fit scenario B) in Figs. 3(c) and 3(d) but larger than the values obtained utilizing fit scenario A (Table I). This can understood by an overestimation of K_{FM} in the case of fitting $H_C^{SW}(\varphi)$ to $H_C^{exp}(\varphi)$ (fit scenario SW) and by an underestimation of K_{FM} in the case of fitting Eq. (11) to $H_C^{exp}(t_{FM})$ (fit scenario A), because $H_C^{exp}(t_{FM})$ values at large t_{FM} are needed to accurately determine the offset $2K_{FM}/\mu_0 M_S$. When fitting Eq. (11) to $H_C^{exp}(t_{AFM})$ (fit scenario C), K_{FM} is determined by values at small t_{AFM}, $t_{AFM} \to 0$, which is more explicit as H_C^{exp} can be measured for $t_{AFM} = 0$ nm by omitting the AFM layer.

Values for μ and σ as well as the expectation value $\langle r_{AFM} \rangle$ of the AFM grain radius and the standard deviation SD extracted by fitting Eqs. (10) and (11) to $|H_{EB}^{exp}(t_{AFM})|$ and $H_C^{exp}(t_{AFM})$ in Fig. 4(a) and Eq. (12) to $J_{eff}(t_{AFM})$ in Fig. 4(c) (Table III, fit scenarios C and J) are listed in Table I. These fit scenarios yield considerably smaller values for $\langle r_{AFM} \rangle$ than the structural average AFM grain radius (7.0 ± 0.3) nm determined by atomic force microscopy. Averaging the obtained values of μ and σ in the case of fit scenario C yields $\langle r_{AFM} \rangle = (3.0 \pm 0.6)$ nm representing $\approx (43 \pm 10)\%$ of the experimentally determined value. This indicates that only about $\approx (18 \pm 8)\%$ of the structural AFM grain volume is effectively contributing to the interfacial exchange coupling. The latter is visualized by comparing the structural ($t_{AFM} = 5$ nm [Fig. 2(e)]) and the magnetically effective distribution of AFM grain radii in Fig. 5(a) and by comparing the structural and magnetically effective AFM GVD for $t_{AFM} = 5$ and 30 nm in Fig. 5(b) with the help of Eq. (2).

It is not surprising that the structural AFM grain volume exceeds the magnetically effective AFM grain volume since the former defines the space over which the AFM order can extend. Thus the difference is expected to arise due to defects or impurities within the individual grains' volume or at the AFM/FM bilayer's interface. Regarding the latter, solely uncompensated AFM moments contribute to the interfacial exchange coupling, for which reason the presence of compensated moments results in an effective reduction in the AFM grains' coupling areas shared with the FM layer. It is important to point out that interfacial roughness or stoichiometric gradients certainly have an impact on the effective coupling constant, just as volume defects influence the AFM grains' magnetic anisotropy. While the former eventually scales the exchange bias shift and the coercive field, the latter specifies the distribution of the AFM grains' energy barriers [48]. The relationship between the distribution of magnetically active and structural grain sizes could therefore be investigated more thoroughly by systematically introducing structural defects only into the volume of the AFM grains, e.g., via light-ion bombardment not penetrating the bilayer's interface [55].

Finally, from the determined grain class boundaries listed in Table I, also the timescales determining these boundaries for fixed temperatures can be derived using Eq. (3). For the grain class boundaries between classes I and II as well as between classes II and III, the respective time scales have been determined to be $\tau_{I/II} = (2 \pm 2) \times 10^{-9}$ s and $\tau_{II/III} = (41 \pm 30)$ s with $T = T_{RT} \approx 293$ K based on the average values of $V_{I/II}$ and $V_{II/III}$ obtained by fitting Eqs. (10) and (11) to $|H_{EB}^{exp}(t_{AFM})|$ and $H_C^{exp}(t_{AFM})$ (Table III, fit scenario C). Despite the rather large uncertainty, the measurement time $t_{Hys} \approx 44$ s is reproduced by $\tau_{II/III}$.

C. Deposition-rate-dependent analysis

Equations (10) and (11) as relations that can be fitted to t_{AFM}-dependent data of the EB shift and the coercivity represent a powerful tool to retrieve parameters characterizing the microstructure of the AFM layer in a polycrystalline EB system. Therefore $|H_{EB}^{exp}(t_{AFM})|$ and $H_C^{exp}(t_{AFM})$ have been experimentally determined for fixed $t_{FM} = 10$ nm for different deposition rates η_{AFM} of the AFM layer to modify the distribution of AFM grain radii [24,26]. $|H_{EB}^{exp}(t_{AFM}, \eta_{AFM})|$ and $H_C^{exp}(t_{AFM}, \eta_{AFM})$ are displayed in Figs. 6(a) and 6(b), respectively, for different η_{AFM}. $|H_{EB}^{exp}(t_{AFM}, \eta_{AFM})|$ and $H_C^{exp}(t_{AFM}, \eta_{AFM})$ are equivalent to the dependencies depicted in Fig. 4(a) for large η_{AFM}, whereas for decreasing η_{AFM} a gradual suppression of the EB shift and the coercivity can be observed [26].

Parameters $\langle r_{AFM} \rangle$, J_{EB}, and K_{FM} as functions of η_{AFM} have been determined by fitting Eqs. (10) and (11) in Figs. 6(a) and 6(b) (Table III, fit scenario C) and are presented in Figs. 6(c)–6(e). In the deposition rate interval in which an overall increase in $|H_{EB}^{exp}(t_{AFM}, \eta_{AFM})|$ and $H_C^{exp}(t_{AFM}, \eta_{AFM})$ can be observed, $\langle r_{AFM} \rangle$ and J_{EB} increase gradually until saturation with $\overline{\langle r_{AFM} \rangle} = (3.0 \pm 0.3)$ nm and $\langle J_{EB} \rangle = (2.2 \pm 0.5) \times 10^{-4}$ J/m^2 for $\eta_{AFM} \geqslant 2.43$ nm/min. K_{FM} stays constant for all η_{AFM} with an average value of $\langle K_{FM} \rangle = (1.4 \pm 0.7)$ kJ/m^3. This implies a constant FUMA independent of η_{AFM} but a dependence of the average AFM grain radius $\langle r_{AFM} \rangle$ and the microscopic coupling constant J_{EB} on the AFM deposition rate for $\eta_{AFM} < 2.43$ nm/min. A reduction in J_{EB} might be connected to an η_{AFM} dependence of the AFM/FM-interface structure or the AFM crystal texture and homogeneity of AFM crystallites, crucially determining the coupling strength between individual AFM grains and the FM [1,3,22,26,56].

D. Simulations and cross-check

In addition to the experimental approach discussed so far, Eqs. (10) and (11) are fitted to $|H_{EB}^{SW}(t_{FM}, t_{AFM})|$ and $H_C^{SW}(t_{FM}, t_{AFM})$, which have been simulated by using the time-dependent SW ansatz given by Eq. (13) (Table III, fit scenario CC). With Eqs. (10) and (11) reproducing the input parameters of the simulations, the validity of the named relations is evidenced (cross-check) in the context of the time-dependent SW approach introduced in Sec. III D and Refs. [26,28,36,48].

The individual steps of the cross-check are shown in Fig. 7 and will be explained in the following. The input parameters used are listed in Table II based on the averaged parameters given in Table I obtained by fitting Eqs. (10) and (11) to $|H_{EB}^{exp}(t_{AFM})|$ and $H_C^{exp}(t_{AFM})$ (Table III, fit scenario C). Starting from the input parameters μ and σ, the AFM GVD $\varrho(V_{AFM}, t_{AFM}, \mu, \sigma)$ can be calculated for different values of t_{AFM} [Eq. (2)]. In Fig. 8(a), calculated AFM GVDs are displayed for exemplary thicknesses t_{AFM} visualizing the tunability of the grain classes' population with the AFM layer thickness. $J_{eff}(t_{AFM})$, $p_{III}(t_{AFM}) = 1 - p_{II}(t_{AFM})$, and consequently $J_{II/III}(t_{AFM})$, as well as $\tau_C^{II}(t_{AFM})$, are determined for fixed J_{EB} and K_{FM} by integration of the AFM GVD considering respective bounds $V_{I/II}$, $V_{II/III}$, and $V_{III/IV}$ given in Table II. With $J_{add} = 0$ J/m^2, $\gamma_{FM} = \gamma_{EB}^{II} = 0°$, and $M_S = 1527$ kA/m, $|H_{EB}^{SW}(t_{FM}, t_{AFM})|$ and $H_C^{SW}(t_{FM}, t_{AFM})$ have been simulated using the time-dependent SW ansatz based on Eq. (13) and are displayed in Figs. 8(b) and 8(d) with fits of Eqs. (10) and

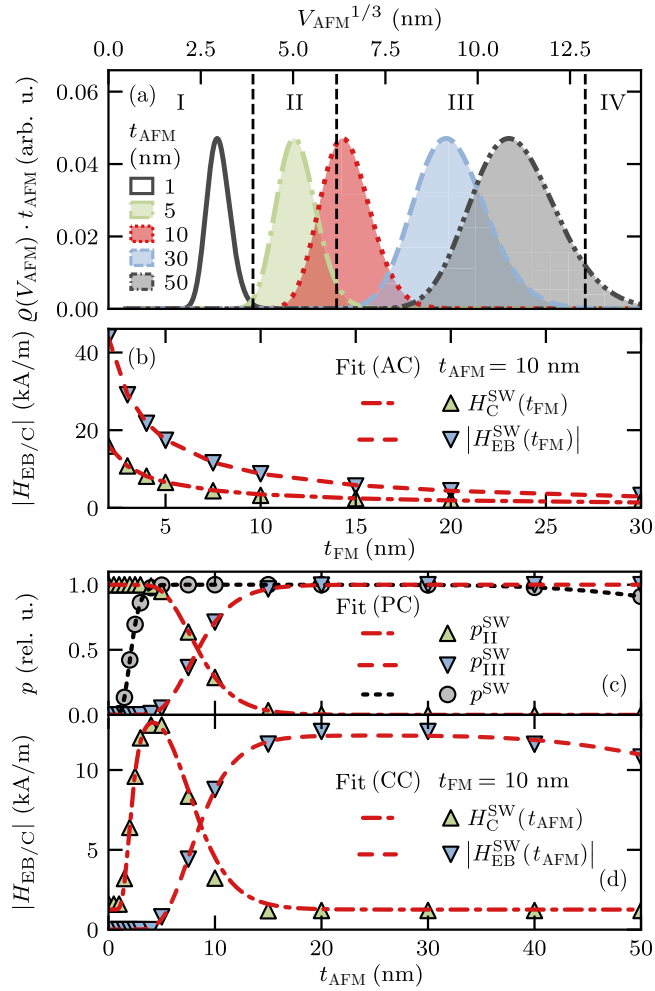

FIG. 8. (a) Calculated AFM GVDs for different values of t_{AFM} based on parameters μ and σ from Table II. (b) Simulated $|H_{EB}^{SW}(t_{FM})|$ and $H_C^{SW}(t_{FM})$ for $t_{AFM} = 10$ nm in (a) with corresponding fits $\propto 1/t_{FM}$ (Table III, fit scenario AC). (c) t_{AFM}-dependent p^{SW} and $p_{III}^{SW} = 1 - p_{II}^{SW}$ obtained by integrating distributions in (a) and corresponding fits based on Eqs. (8) and (9) (Table III, fit scenario PC). (d) Simulated $|H_{EB}^{SW}(t_{AFM})|$ and $H_C^{SW}(t_{AFM})$ using $p^{SW}(t_{AFM})$ and $p_{III}^{SW}(t_{AFM}) = 1 - p_{II}^{SW}(t_{AFM})$ displayed in (c) alongside fits using Eqs. (10) and (11) (Table III, fit scenario CC). Input parameters for (a)–(d) are given in Table II alongside extracted fit parameters.

(11) (Table III, fit scenario CC) for the reproduction of the input parameters as depicted in Fig. 7.

Simulated $|H_{\mathrm{EB}}^{\mathrm{SW}}(t_{\mathrm{FM}})|$ and $H_{\mathrm{C}}^{\mathrm{SW}}(t_{\mathrm{FM}})$ are presented in Fig. 8(b) for $t_{\mathrm{AFM}} = 10$ nm with fits using Eqs. (10) and (11) (Table III, fit scenario AC). The t_{FM}-dependent relations $|H_{\mathrm{EB}}(t_{\mathrm{FM}})|$ and $H_{\mathrm{C}}^{\mathrm{SW}}$ fit well to the simulated $|H_{\mathrm{EB}}^{\mathrm{SW}}(t_{\mathrm{FM}})|$ and $H_{\mathrm{C}}^{\mathrm{SW}}(t_{\mathrm{FM}})$, and the effective coupling constants J_{II} and J_{III} of the respective grain classes are reproduced with a deviation of $\lesssim 10\%$ from the input values (Table II). However, $K_{\mathrm{FM}} = (0.34 \pm 0.07)$ kJ/m^3 differs from the input value 1.21 kJ/m^3 as the offset $2K_{\mathrm{FM}}/\mu_0 M_{\mathrm{S}}$ in Eq. (11) is determined by values of the coercive field at large t_{FM}.

Simulated $p^{\mathrm{SW}}(t_{\mathrm{AFM}})$ and $p_{\mathrm{III}}^{\mathrm{SW}}(t_{\mathrm{AFM}}) = 1 - p_{\mathrm{II}}^{\mathrm{SW}}(t_{\mathrm{AFM}})$ and simulated $|H_{\mathrm{EB}}^{\mathrm{SW}}(t_{\mathrm{AFM}})|$ and $H_{\mathrm{C}}^{\mathrm{SW}}(t_{\mathrm{AFM}})$ are depicted in Figs. 8(c) and 8(d), respectively, which qualitatively reproduce the experimentally determined t_{AFM} dependencies displayed in Figs. 4(a)–4(c). Fits based on Eqs. (8) and (9) (Table III, fit scenario PC) as well as Eqs. (10) and (11) (Table III, fit scenario CC) agree with the simulated dependencies. Within the uncertainty margins, input parameters used for the simulated dependencies are reproduced by fit scenarios PC and CC (Table II).

The agreement of the the relations $|H_{\mathrm{EB}}(t_{\mathrm{FM}}, t_{\mathrm{AFM}})|$ and $H_{\mathrm{C}}(t_{\mathrm{FM}}, t_{\mathrm{AFM}})$ as defined by Eqs. (10) and (11) with the simulated relations $|H_{\mathrm{EB}}^{\mathrm{SW}}(t_{\mathrm{FM}}, t_{\mathrm{AFM}})|$ and $H_{\mathrm{C}}^{\mathrm{SW}}(t_{\mathrm{FM}}, t_{\mathrm{AFM}})$ based on Eq. (13) emphasizes the validity of the direct connection between the SW approach and the presented analytic expressions of the EB shift and the coercivity.

V. CONCLUSION

We conducted a systematic investigation of the ferromagnetic (FM) as well as the antiferromagnetic (AFM) thickness dependence of the exchange bias (EB) shift and the coercive field of the prototypical polycrystalline AFM/FM-bilayer IrMn(t_{AFM})/CoFe(t_{FM}). Thickness-dependent relations, further depending on the conditions of observation and the parameters characterizing the AFM grain volume distribution (GVD), are introduced and validated by the comparison with simulations based on an extended time-dependent Stoner-Wohlfarth (SW) ansatz. These are proved to interlink the averaged microscopic material parameters with averaged macroscopic magnetic quantities, representing an adequate tool to check for the equality of the magnetically effective AFM GVD and the structural AFM GVD.

In contrast to the average structural AFM grain radius (7.0 ± 0.3) nm, experimentally determined by atomic force microscopy, fits to the measured t_{AFM}-dependent EB shift and coercive field gave rise to a significantly smaller value of (3.0 ± 0.6) nm. This indicates that the grains' AFM order extends only over $(18 \pm 8)\%$ of the structural volume, which is hypothesized to be correlated to volume defects within the individual AFM grains.

For the investigated system, the microscopic coupling constant could be determined to be $J_{\mathrm{EB}} = (2.3 \pm 1.7) \times 10^{-4}$ J/m^2 by fitting t_{AFM}-dependent relations of the EB shift and the coercive field to thickness-dependent experimental data, whereas fits based on the time-dependent SW ansatz yielded $J_{\mathrm{EB}} = (2.17 \pm 0.06) \times 10^{-4}$ J/m^2. Furthermore, the timescale of observation for measurements at room temperature could be reproduced, and the timescale below which thermally unstable AFM grains exhibit superparamagnetic behavior could be estimated to be $\tau_{\mathrm{I/II}} = (2 \pm 2) \times 10^{-9}$ s. Introducing the AFM layer's deposition rate as an additional parameter alongside its thickness allowed for a systematic study of the EB shift and the coercive field depending on the average aspect ratio of AFM grains. The extracted averaged microscopic parameters as functions of the deposition rate are in agreement with the utilized model description.

Successfully interlinking analytic expressions describing $|H_{\mathrm{EB}}(t_{\mathrm{FM}}, t_{\mathrm{AFM}})|$ and $H_{\mathrm{C}}(t_{\mathrm{FM}}, t_{\mathrm{AFM}})$ with averaged microscopic material parameters in the context of a generalized model emphasizes the consistency of the latter. The presented overall macroscopic approach for the description of polycrystalline EB bilayers depending on their microstructure represents a showcase example for the modeling of polycrystalline systems in general and especially more complex heterostructures composed of systems similar to the ones investigated.

ACKNOWLEDGMENTS

We acknowledge funding by the DAAD (Project No. 57392264). Furthermore, we thank Dennis Holzinger, André Knie, Feliks Stobiecki, Bogdan Szymański, Piotr Kuświk, and Hubert Głowinski for fruitful discussions and Adam Krysztofik for performing vector network analyzer ferromagnetic resonance measurements.

APPENDIX: FIT SCENARIOS

In this paper, different fits are performed, which are listed in Table III. For each individual scenario, the fit function, the data to be fitted, and the extractable parameters are given.

Fit scenarios A and B represent relations based on Eqs. (10) and (11) introduced in Sec. III C fitted to experimentally determined $|H_{\mathrm{EB}}^{\mathrm{exp}}(t_{\mathrm{FM}})|$ and $H_{\mathrm{C}}^{\mathrm{exp}}(t_{\mathrm{FM}})$ for fixed t_{AFM}, whereas fit scenario C is connected to the same equations, which are, however, fitted to $|H_{\mathrm{EB}}^{\mathrm{exp}}(t_{\mathrm{AFM}})|$ and $H_{\mathrm{C}}^{\mathrm{exp}}(t_{\mathrm{AFM}})$ for fixed t_{FM}. Fit scenario SW describes the fit of angular-resolved model calculations $H_{\mathrm{EB/C}}^{\mathrm{SW}}(\varphi)$ to $H_{\mathrm{EB/C}}^{\mathrm{exp}}(\varphi)$ by minimization of Eq. (13) representative for the time-dependent SW ansatz introduced in Sec. III D, aiming for the quantitative determination of model parameters. Fit scenarios P and J are t_{AFM}-dependent fits of Eqs. (8), (9), and (12) to $p(t_{\mathrm{AFM}})$, $p_{\mathrm{III}}(t_{\mathrm{AFM}}) = 1 - p_{\mathrm{II}}(t_{\mathrm{AFM}})$, and $J_{\mathrm{eff}}(t_{\mathrm{AFM}})$ obtained by fit scenario SW. Fit scenarios AC, PC, and CC are t_{FM}- and t_{AFM}-dependent fits of Eqs. (10), (11), (8), and (9) to $|H_{\mathrm{EB}}^{\mathrm{SW}}(t_{\mathrm{FM}}, t_{\mathrm{AFM}})|$, $H_{\mathrm{C}}^{\mathrm{SW}}(t_{\mathrm{FM}}, t_{\mathrm{AFM}})$, $p^{\mathrm{SW}}(t_{\mathrm{AFM}})$, and $p_{\mathrm{III}}^{\mathrm{SW}}(t_{\mathrm{AFM}}) = 1 - p_{\mathrm{II}}(t_{\mathrm{AFM}})$ obtained by model calculations based on the time-dependent SW ansatz given by Eq. (13) and the calculation of the AFM GVD for a specific set of input parameters (Table II). These fit scenarios are variations of fit scenarios A, P, and C as they are performed for the cross-check between the extended phenomenological relations introduced in Sec. III C and the time-dependent SW ansatz explained in Sec. III D.

TABLE III. Overview of the different fit scenarios referred to in this paper. For each case it is displayed which fit functions with the respective dependencies are used, to which type of data they are fitted, and which fit parameters are extracted. Fit scenarios A, B, C, AC, and CC are based on Eqs. (10) and (11). Fit scenarios P and PC are connected to Eqs. (8) and (9), while fit scenario J is based on Eq. (12). Fit scenario SW represents the fit of model calculations, using the extended time-dependent SW ansatz based on Eq. (13) and introduced in Sec. III D, to experimentally determined angular-resolved data.

Scenario	Fit function	Data to be fitted			Fit parameters
A	$\lvert H_{\mathrm{EB}}(t_{\mathrm{FM}})\rvert = \frac{J_{\mathrm{III}}}{\mu_0 M_{\mathrm{S}} t_{\mathrm{FM}}}$ $H_{\mathrm{C}}(t_{\mathrm{FM}}) = \frac{J_{\mathrm{II}}}{\mu_0 M_{\mathrm{S}} t_{\mathrm{FM}}} + \frac{2K_{\mathrm{FM}}}{\mu_0 M_{\mathrm{S}}}$	$\lvert H_{\mathrm{EB}}^{\mathrm{exp}}(t_{\mathrm{FM}})\rvert$ $H_{\mathrm{C}}^{\mathrm{exp}}(t_{\mathrm{FM}})$	for fixed	$t_{\mathrm{AFM}}, M_{\mathrm{S}}$	$J_{\mathrm{II}}, J_{\mathrm{III}}, K_{\mathrm{FM}}$
B	$\lvert H_{\mathrm{EB}}(t_{\mathrm{FM}})\rvert = \frac{j_{\mathrm{III}}}{\mu_0 M_{\mathrm{S}} t_{\mathrm{FM}}^2}$ $H_{\mathrm{C}}(t_{\mathrm{FM}}) = \frac{j_{\mathrm{II}}}{\mu_0 M_{\mathrm{S}} t_{\mathrm{FM}}^2} + \frac{2K_{\mathrm{FM}}}{\mu_0 M_{\mathrm{S}}}$				$j_{\mathrm{II}}, j_{\mathrm{III}}, K_{\mathrm{FM}}$
C	$\lvert H_{\mathrm{EB}}(t_{\mathrm{AFM}})\rvert = \frac{J_{\mathrm{EB}}\, p(t_{\mathrm{AFM}}, \{V_{\mathrm{I/II}}, V_{\mathrm{III/IV}}, \mu, \sigma\})}{\mu_0 M_{\mathrm{S}} t_{\mathrm{FM}}} \times p_{\mathrm{III}}^{\mathrm{max}}\, p_{\mathrm{III}}(t_{\mathrm{AFM}}, \{V_{\mathrm{II/III}}, V_{\mathrm{III/IV}}, \mu, \sigma\})$ $H_{\mathrm{C}}(t_{\mathrm{AFM}}) = \frac{J_{\mathrm{EB}}\, p(t_{\mathrm{AFM}}, \{V_{\mathrm{I/II}}, V_{\mathrm{III/IV}}, \mu, \sigma\})}{\mu_0 M_{\mathrm{S}} t_{\mathrm{FM}}} \times [1 - p_{\mathrm{III}}^{\mathrm{max}}\, p_{\mathrm{III}}(t_{\mathrm{AFM}}, \{V_{\mathrm{II/III}}, V_{\mathrm{III/IV}}, \mu, \sigma\})] + \frac{2K_{\mathrm{FM}}}{\mu_0 M_{\mathrm{S}}}$	$\lvert H_{\mathrm{EB}}^{\mathrm{exp}}(t_{\mathrm{AFM}})\rvert$ $H_{\mathrm{C}}^{\mathrm{exp}}(t_{\mathrm{AFM}})$	for fixed	$t_{\mathrm{FM}}, M_{\mathrm{S}}$	$J_{\mathrm{EB}}, K_{\mathrm{FM}}$, μ, σ, $V_{\mathrm{I/II}}$, $V_{\mathrm{II/III}}$, $V_{\mathrm{III/IV}}$, $p_{\mathrm{III}}^{\mathrm{max}}$
SW	$H_{\mathrm{EB/C}}^{\mathrm{SW}}(\varphi)$ via $\min_{\beta_{\mathrm{FM}}} \left\{ \frac{E(\beta)}{A} \right\}$	$H_{\mathrm{EB/C}}^{\mathrm{exp}}(\varphi)$	for fixed	$t_{\mathrm{FM}}, t_{\mathrm{AFM}}, M_{\mathrm{S}}$	$p_{\mathrm{III}} = 1 - p_{\mathrm{II}}, \tau_{\mathrm{C}}^{\mathrm{II}}$, $J_{\mathrm{eff}}, J_{\mathrm{add}}, K_{\mathrm{FM}}, \gamma_{\mathrm{FM}}, \gamma_{\mathrm{EB}}^{\mathrm{III}}$
P	$p(t_{\mathrm{AFM}}) = \{\chi(V_{\mathrm{III/IV}}, t_{\mathrm{AFM}}, \mu, \sigma) - \chi(V_{\mathrm{I/II}}, t_{\mathrm{AFM}}, \mu, \sigma)\}/2$ $p_{\mathrm{III}}(t_{\mathrm{AFM}}) = p_{\mathrm{III}}^{\mathrm{max}}\{\chi(V_{\mathrm{III/IV}}, t_{\mathrm{AFM}}, \mu, \sigma) - \chi(V_{\mathrm{II/III}}, t_{\mathrm{AFM}}, \mu, \sigma)\}/2p(t_{\mathrm{AFM}})$	(SW) $p(t_{\mathrm{AFM}})$ $p_{\mathrm{III}}(t_{\mathrm{AFM}})$	for fixed	$t_{\mathrm{FM}}, M_{\mathrm{S}}$	μ, σ, $V_{\mathrm{I/II}}$, $V_{\mathrm{II/III}}$, $V_{\mathrm{III/IV}}$, $p_{\mathrm{III}}^{\mathrm{max}}$
J	$J_{\mathrm{eff}}(t_{\mathrm{AFM}}) = J_{\mathrm{EB}}\, p(t_{\mathrm{AFM}}, \{V_{\mathrm{I/II}}, V_{\mathrm{III/IV}}, \mu, \sigma\})$	(SW) $J_{\mathrm{eff}}(t_{\mathrm{AFM}})$	for fixed	$t_{\mathrm{FM}}, M_{\mathrm{S}}$	J_{EB}, $\mu, \sigma, V_{\mathrm{I/II}}, V_{\mathrm{III/IV}}$
AC	$\lvert H_{\mathrm{EB}}(t_{\mathrm{FM}})\rvert = \frac{J_{\mathrm{III}}}{\mu_0 M_{\mathrm{S}} t_{\mathrm{FM}}}$ $H_{\mathrm{C}}(t_{\mathrm{FM}}) = \frac{J_{\mathrm{II}}}{\mu_0 M_{\mathrm{S}} t_{\mathrm{FM}}} + \frac{2K_{\mathrm{FM}}}{\mu_0 M_{\mathrm{S}}}$	$\lvert H_{\mathrm{EB}}^{\mathrm{SW}}(t_{\mathrm{FM}})\rvert$ $H_{\mathrm{C}}^{\mathrm{SW}}(t_{\mathrm{FM}})$	for input parameters	$J_{\mathrm{EB}}, K_{\mathrm{FM}}$, M_{S}, γ, $\gamma_{\mathrm{EB}}^{\mathrm{III}}$, μ, σ, $V_{\mathrm{I/II}}$, $V_{\mathrm{II/III}}$, $V_{\mathrm{III/IV}}$	$J_{\mathrm{II}}, J_{\mathrm{III}}, K_{\mathrm{FM}}$
PC	$p(t_{\mathrm{AFM}}) = \{\chi(V_{\mathrm{III/IV}}, t_{\mathrm{AFM}}, \mu, \sigma) - \chi(V_{\mathrm{I/II}}, t_{\mathrm{AFM}}, \mu, \sigma)\}/2$ $p_{\mathrm{III}}(t_{\mathrm{AFM}}) = p_{\mathrm{III}}^{\mathrm{max}}\{\chi(V_{\mathrm{III/IV}}, t_{\mathrm{AFM}}, \mu, \sigma) - \chi(V_{\mathrm{II/III}}, t_{\mathrm{AFM}}, \mu, \sigma)\}/2p(t_{\mathrm{AFM}})$	$p^{\mathrm{SW}}(t_{\mathrm{AFM}})$ $p_{\mathrm{III}}^{\mathrm{SW}}(t_{\mathrm{AFM}})$			μ, σ, $V_{\mathrm{I/II}}$, $V_{\mathrm{II/III}}$, $V_{\mathrm{III/IV}}$, $p_{\mathrm{III}}^{\mathrm{max}}$
CC	$\lvert H_{\mathrm{EB}}(t_{\mathrm{AFM}})\rvert = \frac{J_{\mathrm{EB}}\, p(t_{\mathrm{AFM}}, \{V_{\mathrm{I/II}}, V_{\mathrm{III/IV}}, \mu, \sigma\})}{\mu_0 M_{\mathrm{S}} t} \times p_{\mathrm{III}}^{\mathrm{max}}\, p_{\mathrm{III}}(t_{\mathrm{AFM}}, \{V_{\mathrm{II/III}}, V_{\mathrm{III/IV}}, \mu, \sigma\})$ $H_{\mathrm{C}}(t_{\mathrm{AFM}}) = \frac{J_{\mathrm{EB}}\, p(t_{\mathrm{AFM}}, \{V_{\mathrm{I/II}}, V_{\mathrm{III/IV}}, \mu, \sigma\})}{\mu_0 M_{\mathrm{S}} t_{\mathrm{FM}}} \times [1 - p_{\mathrm{III}}^{\mathrm{max}}\, p_{\mathrm{III}}(t_{\mathrm{AFM}}, \{V_{\mathrm{II/III}}, V_{\mathrm{III/IV}}, \mu, \sigma\})] + \frac{2K_{\mathrm{FM}}}{\mu_0 M_{\mathrm{S}}}$	$\lvert H_{\mathrm{EB}}^{\mathrm{SW}}(t_{\mathrm{AFM}})\rvert$ $H_{\mathrm{C}}^{\mathrm{SW}}(t_{\mathrm{AFM}})$			$J_{\mathrm{EB}}, K_{\mathrm{FM}}$, μ, σ, $V_{\mathrm{I/II}}$, $V_{\mathrm{II/III}}$, $V_{\mathrm{III/IV}}$, $p_{\mathrm{III}}^{\mathrm{max}}$

[1] J. Nogués and I. K. Schuller, J. Magn. Magn. Mater. **192**, 203 (1999).

[2] W. H. Meiklejohn, J. Appl. Phys. (Melville, NY) **33**, 1328 (1962).

[3] K. O'Grady, L. E. Fernandez-Outon, and G. Vallejo-Fernandez, J. Magn. Magn. Mater. **322**, 883 (2010).

[4] P. Sharma, E. Albisetti, M. Monticelli, R. Bertacco, and D. Petti, Sensors **16**, 1030 (2016).

[5] H. W. Chang, Y. H. Chien, F. T. Yuan, Y. R. Lai, C. R. Wang, L. Horng, and W. C. Chang, AIP Adv. **10**, 025035 (2020).

[6] O. Manos, P. Bougiatioti, D. Dyck, T. Huebner, K. Rott, J. M. Schmalhorst, and G. Reiss, J. Appl. Phys. (Melville, NY) **125**, 023905 (2019).

[7] C. Binek, A. Hochstrat, X. Chen, P. Borisov, W. Kleemann, and B. Doudin, J. Appl. Phys. (Melville, NY) **97**, 10C514 (2005).

[8] A. Ehresmann, D. Junk, D. Engel, A. Paetzold, and K. Röll, J. Phys. D: Appl. Phys. **38**, 801 (2005).

[9] A. Gaul, S. Hankemeier, D. Holzinger, N. D. Müglich, P. Staeck, R. Frömter, H. P. Oepen, and A. Ehresmann, J. Appl. Phys. (Melville, NY) **120**, 033902 (2016).

[10] A. Gaul, D. Emmrich, T. Ueltzhöffer, H. Huckfeldt, H. Doganay, J. Hackl, M. I. Khan, D. M. Gottlob, G. Hartmann, A. Beyer, D. Holzinger, S. Nemšák, C. M. Schneider, A. Gölzhäuser, G. Reiss, and A. Ehresmann, Beilstein J. Nanotechnol. **9**, 2968 (2018).

[11] Y. Q. Zhang, X. Z. Ruan, B. Liu, Z. Y. Xu, Q. Y. Xu, J. D. Shen, Q. Li, J. Wang, B. You, H. Q. Tu, Y. Gao, W. Zhang, Y. B. Xu, and J. Du, Appl. Surf. Sci. **367**, 418 (2016).

[12] I. Berthold, U. L. Oschner, J. Schille, R. Ebert, and H. Exner, Phys. Procedia **56**, 1136 (2014).

[13] E. Albisetti, D. Petti, M. Pancaldi, M. Madami, S. Tacchi, J. Curtis, G. Csaba, W. Porod, P. Vavassori, E. Riedo, and R. Bertacco, Nat. Nanotechnol. **11**, 545 (2016).

[14] A. Ehresmann, I. Koch, and D. Holzinger, Sensors **15**, 28854 (2015).

[15] M. Reginka, H. Hoang, O. Efendi, M. Merkel, R. Huhnstock, D. Holzinger, K. Dingel, B. Sick, D. Bertinetti, F. Herberg, and A. Ehresmann, Langmuir **37**, 8498 (2021).

[16] R. Huhnstock, M. Reginka, A. Tomita, M. Merkel, K. Dingel, D. Holzinger, B. Sick, M. Vogel, and A. Ehresmann, Sci. Rep. **11**, 21794 (2021).

[17] D. Holzinger, I. Koch, S. Burgard, and A. Ehresmann, ACS Nano **9**, 7323 (2015).

[18] F. Radu and H. Zabel, in *Magnetic Heterostructures Advances and Perspectives in Spinstructures and Spintransport*, Springer Tracts in Modern Physics Vol. 227 (Springer, New York, 2008), pp. 97–184.

[19] J. Geshev, L. G. Pereira, and J. E. Schmidt, Phys. Rev. B **66**, 134432 (2002).

[20] A. E. Berkowitz and K. Takano, J. Magn. Magn. Mater. **200**, 552 (1999).

[21] A. P. Malozemoff, Phys. Rev. B **35**, 3679 (1987).

[22] N. P. Aley, G. Vallejo-Fernandez, R. Kroeger, B. Lafferty, J. Agnew, Y. Lu, and K. O'Grady, IEEE Trans. Magn. **44**, 2820 (2008).

[23] A. Kohn, A. Kovács, R. Fan, G. J. McIntyre, R. C. Ward, and J. P. Goff, Sci. Rep. **3**, 2412 (2013).

[24] M. Vopsaroiu, G. V. Fernandez, M. J. Thwaites, J. Anguita, P. J. Grundy, and K. O'Grady, J. Phys. D: Appl. Phys. **38**, 490 (2005).

[25] A. Harres and J. Geshev, J. Phys.: Condens. Matter **24**, 326004 (2012).

[26] M. Merkel, R. Huhnstock, M. Reginka, D. Holzinger, M. Vogel, A. Ehresmann, J. Zehner, and K. Leistner, Phys. Rev. B **102**, 144421 (2020).

[27] E. Fulcomer and S. H. Charap, J. Appl. Phys. (Melville, NY) **43**, 4190 (1972).

[28] N. D. Müglich, A. Gaul, M. Meyl, A. Ehresmann, G. Götz, G. Reiss, and T. Kuschel, Phys. Rev. B **94**, 184407 (2016).

[29] M. Ali, C. H. Marrows, M. Al-Jawad, B. J. Hickey, A. Misra, U. Nowak, and K. D. Usadel, Phys. Rev. B **68**, 214420 (2003).

[30] M. Ali, C. H. Marrows, and B. J. Hickey, Phys. Rev. B **67**, 172405 (2003).

[31] L. Alonso, T. R. Peixoto, and D. R. Cornejo, J. Phys. D: Appl. Phys. **43**, 465001 (2010).

[32] R. L. Rodríguez-Suárez, A. B. Oliveira, F. Estrada, D. S. Maior, M. Arana, O. Alves Santos, A. Azevedo, and S. M. Rezende, J. Appl. Phys. (Melville, NY) **123**, 043901 (2018).

[33] C. Leighton, M. R. Fitzsimmons, A. Hoffmann, J. Dura, C. F. Majkrzak, M. S. Lund, and I. K. Schuller, Phys. Rev. B **65**, 064403 (2002).

[34] D. Nečas and P. Klapetek, Cent. Eur. J. Phys. **10**, 181 (2012).

[35] F. Radu, A. Westphalen, K. Theis-Bröhl, and H. Zabel, J. Phys.: Condens. Matter **18**, L29 (2006).

[36] M. Merkel, R. Huhnstock, M. Reginka, M. Vogel, A. Ehresmann, H. Glowinski, and P. Kuswik, Phys. Rev. B **104**, 214406 (2021).

[37] G. Vallejo-Fernandez, L. E. Fernandez-Outon, and K. O'Grady, Appl. Phys. Lett. **91**, 212503 (2007).

[38] P. Kuświk, A. Gaul, M. Urbaniak, M. Schmidt, J. Aleksiejew, A. Ehresmann, and F. Stobiecki, Nanomaterials **8**, 813 (2018).

[39] J. Juraszek, J. Fassbender, S. Poppe, T. Mewes, B. Hillebrands, D. Engel, A. Kronenberger, A. Ehresmann, and H. Schmoranzer, J. Appl. Phys. (Melville, NY) **91**, 6896 (2002).

[40] A. Mougin, T. Mewes, M. Jung, D. Engel, A. Ehresmann, H. Schmoranzer, J. Fassbender, and B. Hillebrands, Phys. Rev. B **63**, 060409(R) (2001).

[41] S. W. Kim, S. D. Choi, D. H. Jin, K. A. Lee, S. S. Lee, and D. G. Hwang, J. Magn. Magn. Mater. **272**, 376 (2004).

[42] G. Vallejo-Fernandez, N. P. Aley, J. N. Chapman, and K. O'Grady, Appl. Phys. Lett. **97**, 222505 (2010).

[43] M. Vopsaroiu, M. J. Thwaites, G. V. Fernandez, S. Lepadatu, and K. O'Grady, J. Optoelectron. Adv. Mater. **7**, 2713 (2005).

[44] M. Vopsaroiu, M. Georgieva, P. J. Grundy, G. V. Fernandez, S. Manzoor, M. J. Thwaites, and K. O'Grady, J. Appl. Phys. (Melville, NY) **97**, 10N303 (2005).

[45] N. Balakrishnan and W. W. S. Chen, *Handbook of Tables for Order Statistics from Lognormal Distributions with Applications* (Springer, Boston, 1999).

[46] W. H. Meiklejohn and C. P. Bean, Phys. Rev. **105**, 904 (1957).

[47] J. Muñoz, J. Nogués, J. Sort, V. Langlais, M. Baró, S. Suriñach, and V. Skumryev, Phys. Rep. **422**, 65 (2005).

[48] N. D. Müglich, M. Merkel, A. Gaul, M. Meyl, G. Götz, G. Reiss, T. Kuschel, and A. Ehresmann, New J. Phys **20**, 053018 (2018).

[49] S. Nieber and H. Kronmüller, Phys. Status Solidi B **165**, 503 (1991).

[50] M. Goto, H. Tange, and T. Kamimori, J. Magn. Magn. Mater. **62**, 251 (1986).

[51] D. Mauri, E. Kay, D. Scholl, and J. K. Howard, J. Appl. Phys. (Melville, NY) **62**, 2929 (1987).

[52] J. G. Hu, G. J. Jin, and Y. Q. Ma, J. Appl. Phys. (Melville, NY) **94**, 2529 (2003).

[53] D. V. Dimitrov, S. Zhang, J. Q. Xiao, G. C. Hadjipanayis, and C. Prados, Phys. Rev. B **58**, 12090 (1998).

[54] M. D. Stiles and R. D. McMichael, Phys. Rev. B **63**, 064405 (2001).

[55] A. C. Basaran, T. Saerbeck, J. De La Venta, H. Huckfeldt, A. Ehresmann, and I. K. Schuller, Appl. Phys. Lett. **105**, 072403 (2014).

[56] P. B. Barna and M. Adamik, Thin Solid Films **317**, 27 (1998).